










Submillimeter-wavelength Polarimetry of IRC+10216

B-G. Andersson^{1,2} , Janik Karoly³ , Pierre Bastien⁴ , Archana Soam^{2,5} , Simon Coudé^{2,6,7} , Mehrnoosh Tahani^{8,9,12,13} ,
Michael S. Gordon¹⁰ , and Sydney Fox-Middleton^{2,11}

¹ Institute for Scientific Research, Boston College, 140 Commonwealth Avenue, Chestnut Hill, MA 02467, USA

² SOFIA Science Center, Universities Space Research Association, NASA Ames Research Center, M.S. N232-12, Moffett Field, CA 94035, USA

³ Jeremiah Horrocks Institute, University of Central Lancashire, Preston, PR1 2HE, UK

⁴ Institut de Recherche sur les Exoplanètes (iREx) & Centre de Recherche en Astrophysique du Québec (CRAQ), Université de Montréal, Département de Physique, 1375, Avenue Thérèse-Lavoie-Roux, Montréal, QC, H2V 0B3, Canada

⁵ Indian Institute of Astrophysics, II Block, Koramangala, Bengaluru 560034, India

⁶ Department of Earth, Environment, and Physics, Worcester State University, Worcester, MA 01602, USA

⁷ Center for Astrophysics | Harvard & Smithsonian, 60 Garden Street, Cambridge, MA 02138, USA

⁸ Kavli Institute for Particle Astrophysics & Cosmology (KIPAC), Stanford University, Stanford, CA 94305, USA

⁹ Dominion Radio Astrophysical Observatory, Herzberg Astronomy and Astrophysics Research Centre, National Research Council Canada, P.O. Box 248, Penticton, BC V2A 6J9, Canada

¹⁰ Ball Aerospace, 1600 Commerce Street, Boulder, CO 80301, USA

¹¹ Physics Department, Santa Clara University, 500 El Camino Real, Santa Clara, CA 95053, USA

Received 2021 October 4; revised 2023 December 15; accepted 2023 December 19; published 2024 February 29

Abstract

We present SCUBA-2/POL-2 850 μm polarimetric observations of the circumstellar envelope (CSE) of the carbon-rich asymptotic giant branch (AGB) star IRC+10216. Both far-IR (FIR) and optical polarization data indicate grains aligned with their long axis in the radial direction relative to the central star. The 850 μm polarization does not show this simple structure. The 850 μm data are indicative, albeit not conclusive, of a magnetic dipole geometry. Assuming such a simple dipole geometry, the resulting 850 μm polarization geometry is consistent with both Zeeman observations and small-scale structure in the CSE. While there is significant spectral-line polarization contained within the SCUBA-2 850 μm passband for the source, it is unlikely that our broadband polarization results are dominated by line polarization. To explain the required grain alignment, grain mineralogy effects, due to either fossil silicate grains from the earlier oxygen-rich AGB phase of the star or due to the incorporation of ferromagnetic inclusions in the largest grains, may play a role. We argue that the most likely explanation is due to a new alignment mechanism wherein a charged grain, moving relative to the magnetic field, precesses around the induced electric field and therefore aligns with the magnetic field. This mechanism is particularly attractive as the optical, FIR, and submillimeter-wave polarization of the carbon dust can then be explained in a consistent way, differing simply due to the charge state of the grains.

Unified Astronomy Thesaurus concepts: [Circumstellar dust \(236\)](#); [Magnetic fields \(994\)](#); [Carbonaceous grains \(201\)](#); [Asymptotic giant branch stars \(2100\)](#)

1. Introduction

Visual-light interstellar medium (ISM) polarization was discovered in 1949 (Hall 1949; Hiltner 1949a, 1949b), and from the start hypothesized to be associated with dichroic extinction by asymmetric dust grains aligned with the Galactic magnetic field. The corresponding emission polarization was first detected by Cudlip et al. (1982). Observations of dust-induced polarization covering the UV-to-submillimeter¹⁴ wavelength range serve as efficient probes of both the geometry and strength of the interstellar magnetic fields (e.g., Davis 1951; Chandrasekhar & Fermi 1953; Houde et al. 2009; Lazarian et al. 2022), being widely observable with modest telescope


size and observing time and straightforward to calibrate. The general association of dust polarization with magnetic fields has been securely established, and the general mechanism of the grain alignment is now understood as being radiation driven (see Andersson et al. 2015, henceforth ALV15), but with many details still needing to be explored in detail.

A quantitative theory of grain alignment based on radiative torques has been refined and tested over the last few decades (e.g., Dolginov & Mitrofanov 1976; Draine & Weingartner 1996; Lazarian & Hoang 2007; ALV15). This radiative alignment torque (RAT) theory predicts that the transfer of angular momentum from photons with wavelengths less than the grain diameter ($\lambda < 2a$, where a is the effective grain radius) will spin up an irregular grain.¹⁵ For a paramagnetic grain, some of the rotational energy is exchanged for spin-flips in the solid (the “Barnett effect”; Purcell 1979). This both causes the angular momentum of the grain to align with the grain’s axis of maximum inertia, so-called “internal alignment,” through Barnett dissipation (see Purcell 1979; Lazarian & Draine 1999) and, in steady state, magnetizes the grain. The magnetized grain then Larmor precesses around the external

¹² Banting and KIPAC Fellow.

¹³ Covington Fellow.

¹⁴ For the purposes of the present paper, we will distinguish between far-IR and submillimeter wave, as the former covering the wavelength range where the atmosphere is fully opaque from the ground, i.e., $\lambda \approx 30\text{--}300 \mu\text{m}$, and the latter being $\lambda \approx 350 \mu\text{m}\text{--}1 \text{ mm}$. In practice, here, the distinction is between SOFIA/HAWC+ and JCMT/SCUBA-2/POL-2 or ALMA observations.

 Original content from this work may be used under the terms of the [Creative Commons Attribution 4.0 licence](#). Any further distribution of this work must maintain attribution to the author(s) and the title of the work, journal citation and DOI.

¹⁵ The coupling to the radiation field does not fully cease at $\lambda > 2a$, but falls with a steep dependence (see Hoang et al. 2021).

magnetic field (B field), and continued radiative torques align the grains with the B field (so called “B-RAT”). This paradigm has now been well tested, including observations of a correlation with the radiation intensity (Medan & Andersson 2019; Santos et al. 2019; Soam et al. 2021), a correlation of aligned dust grain size with opacity into a cloud (Andersson & Potter 2007; Vaillancourt et al. 2020), a dependence on the angle between the radiation and the B fields (Andersson et al. 2011; Vaillancourt & Andersson 2015), and a loss of the grain alignment in the starless cores (Alves et al. 2014; Jones et al. 2015; ALV15). However, several detailed aspects of the RAT paradigm are still in need of further clarification.

In particular, the role of grain mineralogy, and the influence of gas-grain relative velocities, remain to be fully understood. With “mineralogy” we here refer to the composition and structure of the solid, as it influences particularly the magnetic properties (dia-, para-, or ferromagnetism) of the grains. One observational effect, related to the grain mineralogy, still needing to be fully understood is why carbonaceous grains appear not to be aligned in the ISM.

While the silicate feature at $\sim 9.7 \mu\text{m}$ shows significant polarization (Smith et al. 2000), the aliphatic CH feature at $3.4 \mu\text{m}$ does not (Chiar et al. 2006). As shown by Chiar et al. (2013), carbon grains will, when exposed to atomic hydrogen and UV radiation, develop CH bonds on their surfaces. The lack of polarization in the $3.4 \mu\text{m}$ feature therefore implies that carbonaceous grains are not aligned with any external reference direction in the ISM.

Chiar et al. (2006) also addressed the possibility, and behavior, of composite grains by comparing the fractional polarization (p/τ), where p is the polarization in the line and τ is the opacity in the (Stokes I) absorption line, in the silicate and CH features toward the Quintuplet cluster members GCS 3-II and 3-IV. They find that the upper limits on $(p/\tau)_{\text{CH}}$ compared with the measured values for $(p/\tau)_{\text{sil}}$ argues against the model of composite grains with a silicate core and organic refractory mantles, and conclude that “the agent responsible for the hydrocarbon feature in the diffuse ISM is located in a grain population that is both physically separate from the silicates and far less efficient as a producer of polarization.”

Recent theoretical work (Draine & Hensley 2021) argues, however, that the observational constraints on the CH feature polarization are just above the expected level of polarization from composite grains consisting of a mix of amorphous silicates and other materials—so-called “astrodust”—provided that the $3.4 \mu\text{m}$ absorption is preferentially located in grain surface layers. Constraining the alignment characteristics of pure carbon dust therefore would be a valuable constraint on ISM modeling.

The nondetection of polarization in the $3.4 \mu\text{m}$ line is consistent with the far-IR (FIR)/submillimeter polarization spectrum models of Draine & Fraisse (2009), which requires two dust components, a cooler aligned one and a warmer unaligned one. Aligned silicate and unaligned carbon grains would explain the FIR/submillimeter-wave polarization spectrum measured by Vaillancourt et al. (2008). We note, however, that recent observations (e.g., Ashton et al. 2018) do not see the distinct concave spectrum discussed by Vaillancourt et al. (2008).

As noted above, two kinds of alignment in dust grains are required to cause polarization. “Internal alignment” is accomplished when the grain spins around one of its principal axes

(usually the axis of maximal inertia = smallest axis; the lowest-energy state for a given total angular momentum), yielding a constant projected shape of that grain. Under angular momentum conservation, internal alignment requires efficient energy dissipation in the grain bulk, which Purcell (1979) showed was most efficiently accomplished through Barnett relaxation in paramagnetic grains (see Lazarian & Draine 1999). “External alignment” signifies the alignment of the individual grains’ spin axes with an external reference direction, *usually* the B field. Both types of alignment assume paramagnetic solids, which in the ISM applies to silicate grains. Carbon grains are, however, diamagnetic and expected to show neither fast internal alignment nor to respond to magnetic fields.

Variants of RAT alignment are also possible, dependent on the radiation field strength and the grain mineralogy. For grains with efficient internal alignment exposed to strong, highly anisotropic radiation fields, the external alignment direction is expected to change to the radiation field propagation direction (its k -vector; so-called “ k -RATs”). This phenomenon may have been detected in the Orion region (Chuss et al. 2019; Pattle et al. 2021) and possibly in protostellar disks (Kataoka et al. 2017).

RAT theory *does* predict that also carbonaceous grains are spun up by an anisotropic radiation field (as seen in the laboratory by Abbas et al. 2006). Hoang & Lazarian (2009) have shown that for strong and anisotropic enough radiation fields, grains without internal alignment can experience a second-order k -RAT alignment. Such alignment is likely to be weak and bimodal, with some grains oriented with their minor axis along the radiation field direction and some with the major axis in that direction. In regions with supersonic gas-grain drift, this drift can preferentially randomize the former grain orientation, because of the larger cross section toward the flow, leaving a net alignment of grains with their long axis in the gas-dust flow direction, thus causing polarization.

As discussed recently by Lazarian (2020), a new alignment mechanism should exist for (i) charged carbon grains with (ii) a net velocity perpendicular to the magnetic field. Such grains get aligned via precession of their electric dipole moment around the induction electric field ($\mathbf{E} \propto \mathbf{v}_{\text{grain}} \times \mathbf{B}$). Both of the required conditions are likely fulfilled in the *outer* envelope of asymptotic giant branch (AGB) star winds, due to the radiative driving of the dust in the AGB wind, and the photoelectric grain charging by the UV light in the interstellar radiation field. As noted by Lazarian (2020), for inherently magnetically active grains (paramagnetic or stronger) B-RATs would, in most situations, dominate this mechanism. Hence, such “E-RAT” alignment is observationally expected to be associated with carbon grains. This electrically induced radiative alignment can cause the grains to align with either their long or short axis along the induced electric field, depending on the relative precession rate around the electrical and magnetic fields: Ω_E and Ω_B . This ratio is given by (Lazarian 2020, Equation (9))

$$\frac{\Omega_E}{\Omega_B} = \frac{p_{\text{el},J} V_{\text{grain}\perp}}{\mu c}, \quad (1)$$

where $p_{\text{el},J}$ is the grain’s electric dipole moment parallel to its angular momentum, $V_{\text{grain}\perp}$ is the grain’s velocity perpendicular to the direction of the magnetic field, and μ is the grain’s magnetic moment.

As shown by Lazarian (2020, their Table 1, and Section 6.2), if the precession rate around the E or B fields (Ω_E) are faster

than around the radiation field direction (Ω_k), then, if $\Omega_E > \Omega_B$, theory predicts that the observed emission polarization should be parallel to the B field (opposite to the situation in interstellar, B-RAT, alignment). If the precession rate around the B field (Ω_B) is faster, the polarization will be perpendicular to the B field (see Lazarian 2020 for details). Therefore, in addition to probing for the magnetic field geometry, such alignment would provide a measure of the microphysics (including charging) of the grains.

In the general ISM, silicate and carbonaceous dust are generally well mixed, making it very difficult to decisively probe this effect, even in environments, such as shock fronts, where systematic supersonic gas-dust drift may exist (Hoang & Lee 2020). We have therefore initiated a program of observations targeting grain alignment in the chemically segregated environments of AGB star envelopes using FIR and submillimeter-wave emission from the circumstellar envelope (CSE), and optical polarimetry observations of background stars.

As medium-mass stars first ascend the AGB, their CSEs reflect the cosmic carbon-to-oxygen abundance ratio $[C]/[O]$ of <1 . Because of the chemical stability of the CO molecule, all the carbon in these oxygen-rich CSEs is then tied up in that gas-phase molecule and the dust formed consists of silicates and metal oxide grains (Gail & Sedlmayr 2013). As the thermal pulses of the later AGB evolution progress (Lattanzio & Wood 2004), newly synthesized carbon is dredged up to the stellar surface and ejected into the CSE, increasing the $[C]/[O]$ ratio to unity (so called S-type stars) and eventually to >1 when the star becomes C-rich (Whittet 2003; Olofsson 2004). The gas is now depleted of oxygen (which is tied up in CO), and the dust formed consists of various forms of carbon solids, including amorphous carbon and silicon carbide (e.g., Ivezić & Elitzur 1996a).

Observations of the planetary nebula BD+30°3639 show that the size of the object at wavelengths dominated by silicate features is larger than that at wavelengths dominated by carbonaceous spectral features (Guzman-Ramirez et al. 2015), indicating that the O-rich to C-rich history of the shell may, in some sources, be traced through high-resolution observations.

IRC+10216 is a well known IR object discovered in 1969 by Eric Becklin (Becklin et al. 1969) and identified as a dust-enshrouded carbon star the following year (Miller 1970). At a distance of only $d = 123 \pm 14$ pc (Groenewegen et al. 2012), it can be resolved by many telescopes, and it has been extensively studied both in continuum and line radiation (e.g., Cernicharo et al. 2010; Decin et al. 2011, and references therein). The extensive dust and gas circumstellar shell ends in a termination shock, where the CSE runs into the ISM, seen in both the UV (Sahai & Chronopoulos 2010) and the FIR (Ladjal et al. 2010). The effective extent of the CSE of IRC+10216 depends on the wavelength of observation and its depth. For reference, the CSE can be detected in visible light (azimuthally averaged to $\sim 200''$; Maun & Huggins 2000), the $70 \mu\text{m}$ extended emission can be detected to at least $285''$ (Dharmawardena et al. 2018) and the asymmetric astrosphere is located at $\sim 500''$ – $600''$ (Sahai & Chronopoulos 2010) from the central star.

With a high C/O ratio (C/O = 1.4; Winters et al. 1994; Milam et al. 2009, and references therein), the dust is fully carbonaceous, consisting of 95% amorphous carbon and 5% SiC by mass (Ivezić & Elitzur 1996a). While iron is found to be

significantly depleted in the gas phase of the CSE (Maun & Huggins 2010), no direct observational evidence for iron grains or iron inclusions in the carbon grains has been found.

Evidence for magnetic fields in the IRC+10216 CSE come from observations of the Goldreich–Kylafis (G-K) effect in several molecules (Girart et al. 2012) with the Submillimeter Array (SMA), and from Zeeman observation in the $J = 1-0$ line of CN (Duthu et al. 2017) with the IRAM 30 m telescope. The G-K observations on small scales indicate a “global radial pattern” (Girart et al. 2012). However, the CN Zeeman observation shows significant spatial variations (including field direction reversals) in the line-of-sight field strength around the star, indicating deviations from spherical symmetry. Hence, while there are strong indications of a magnetic field in the CSE, the geometry of the field is not fully clear. Evidence for simple dipole geometries in AGB star CSEs come, for instance, from Szymczak et al. (2001), using OH maser emission, and Vlemmings et al. (2005), using H₂O masers. Both find that the magnetic field on hundreds to thousands of au scales in the AGB star VX Sgr (Taberero et al. 2021) can be modeled as resulting from a dipole.

For sources such as AGB stars, observed with unresolved aperture or centered-slit polarimetry, asymmetries in the dust distribution and grain alignment effects are very difficult to separate. Kahane et al. (1997) and Bastien (2003) acquired spatially unresolved aperture polarimetry of a sample of 68 AGB stars in a band centered at $0.883 \mu\text{m}$. They divided their sample into two groups, spherical and aspherical envelopes, based on their CO line profiles. Both polarization and CO line profiles can reveal the presence of nonspherical envelopes. No statistical difference was found in polarization histograms of stars with “normal” (spherical) and “abnormal” (aspherical) CO line profiles (Kahane et al. 1997). However, the polarization data showed a significant difference between C-rich and O-rich envelopes, with C-rich CSEs presenting a higher polarization than their O-rich counterparts (Kahane et al. 1997; Bastien 2003), indicating a more asymmetric dust distribution in the former. Biegging et al. (2006) performed optical (0.42 – $0.84 \mu\text{m}$) spectropolarimetry of 21 AGB stars, 13 protoplanetary nebulae, and two R CrB-type stars. They also found a higher fraction of polarization for the carbon-rich AGB stars (five of six) than for the oxygen-rich stars (eight of 14), which they attributed to the later developmental stage of the carbon-rich stars. All of these observations are, however, likely dominated by scattering polarization. High-resolution, active-optics-supported observations in the optical and near-IR can resolve the inner part of the CSEs (e.g., Kastner & Weintraub 1994, 1996; Jeffers et al. 2014; Khouri et al. 2020; Montargès et al. 2023) and provide important information about the spatial dust distribution and grain-size distribution. However, since these observations are dominated by (Rayleigh) scattering, they do not provide information about the grain alignment. In most radiative-transfer modeling of these kinds of data, (e.g., Montargès et al. 2023) the grains are either assumed to be symmetrical or have a random spatial orientation. However, imaging FIR and submillimeter-wave observations can resolve the CSEs and differentiate between the two mechanisms of polarization (scattering and dichroic emission), as the emission wavelengths are much larger than the grain sizes. Similarly, optical polarimetry of background stars with careful subtraction of the diffuse, scattered light from the CSEs can show how the grains are aligned.

IRC+10216 has been previously observed at multiple wavelengths in scattering, dichroic extinction, and emission polarization. Optical through near-IR polarization observation of the central part of the CSE has been reported by, for example, Dyck et al. (1971), Cohen & Schmidt (1982), and Trammell et al. (1994), showing significant polarization rising to the blue (40% at $0.67\ \mu\text{m}$; Cohen & Schmidt 1982), consistent with Rayleigh (dust) scattering. The small-scale dust distribution ($2''$ – $3''$ scales, and hence much smaller than the beams in our studies) has also been extensively studied in recent years. Kastner & Weintraub (1994, 1996) mapped the large-scale structure of the CSE at the J , H , and K bands, while Murakawa et al. (2005), using $2\ \mu\text{m}$ polarization, found a NW–SE structure that they identified as a possible dust torus. Optical broadband polarimetry (Jeffers et al. 2014) reveals a similar structure, which is also consistent with multi-epoch Hubble Space Telescope imaging (Kim et al. 2021). In an accompanying paper (B-G. Andersson et al. 2024, in preparation; Andersson et al. 2018),¹⁶ we discuss the polarimetry of background stars shining through the CSE. While we detect strong scattered light polarization, we can, with careful sky subtraction, also determine the dichroic extinction polarization toward these stars.

Our SOFIA/HAWC+ observations at $53\ \mu\text{m}$ (at $5''$ resolution; Andersson et al. 2022) show a uniform radial polarization for IRC+10216. The FIR polarization maps at 154 and $214\ \mu\text{m}$ also show predominantly radial polarization, albeit with lower signal-to-noise ratio (S/N) and at worse resolution. A tight correlation between the FIR polarization and dust temperature indicates radiative grain alignment, via the second-order k-RAT process discussed above. The low polarization efficiency seen in the inner parts of the $850\ \mu\text{m}$ data presented here (Figure 10) is consistent with k-RAT alignment of grains with no (or slow) internal alignment (Hoang & Lazarian 2009).

Here, we present new James Clerk Maxwell Telescope (JCMT)/SCUBA-2/POL-2 observations of the IRC+10216 CSE and analyze these in the context of SOFIA/HAWC+ and optical polarimetry (as well as other archival data sets) and the general RAT grain alignment paradigm. Along with Andersson et al. (2022), this paper is the start of a comprehensive study, which we have named the Survey of Polarization in AGB Circumstellar Envelopes (or SPACE). We are working to complement the studies of IRC+10216 with observations of the O-rich and S-type AGB stars IK Tau and W Aql.

The paper is structured as follows. We present the observations and data-reduction method in Section 2. Section 3 introduces the analysis of our results; Section 4 summarizes these; before Section 5, where we discuss our results and possible alignment mechanisms. Finally, we summarize our findings in Section 6.

2. Observations and Data Reduction

IRC+10216 was observed with the SCUBA-2/POL-2 instrument combination (Bastien et al. 2011; Holland et al. 2013) on the JCMT, during 2018 January 11 and 12. Six observations lasting 41 minutes each of IRC+10216 were carried out. The regular POL-CV daisy pattern for SCUBA-2/POL-2 covers the star and all of its CSE well. We acquired 12 such patterns to reach a sensitivity of about $3\ \text{mJy beam}^{-1}$ in

polarized intensity in $8\ \text{arcsec}^2$ pixels. Six additional observations were acquired in flexible mode on January 19. We have also included eight repeats that are ~ 31.5 minutes long from archival observations on CADC (Project ID: M19BP001; PI: P. Scicluna).¹⁷

During one observation on January 11, the telescope reached an elevation of 83° . However, upon inspection of the data from that observation, no distortions of the data due to the JCMT alt-azimuth mount could be detected. The membrane in front of the telescope, in regular observations, was removed during the period 2017 December 5 to 2018 January 10 to carry out commissioning tests targeted at better characterizing the instrumental polarization due to the telescope and membrane. The data for this project were, therefore, acquired just after the reinstallation of the Gore-Tex membrane in front of the telescope. Comparison of the instrumental polarization after the membrane was reinstalled with those before it was removed showed no significant differences.

IRC+10216 was previously observed with the earlier JCMT submillimeter-wave polarimeter SCUPOL. These observations were reprocessed, combined, and presented by Matthews et al. (2009). Because these data were of lower S/N, we have not included them in the present analysis.

We reduced the JCMT/POL-2 $850\ \mu\text{m}$ observations using the `pol2map` command of the SMURF package (Chapin et al. 2011) in the Starlink software (Currie et al. 2014). In the first step, using `pol2map`, the Stokes I , Q , and U time streams are separated from the raw observations using the `calcqu` command. Then, the Stokes I time streams are processed using the command `makemap` to produce an initial Stokes I map. This Stokes I map is used as a fixed-S/N mask for the second step of the reduction, where final Stokes I , Q , and U maps are made. The second step consists of running `pol2map` again, however we use `skyloop`¹⁸ to make the final maps rather than `makemap`. `Skyloop` is an iterative map-making command that reduces the growth of large-scale structures that may form due to the map-making routine by combining all the observations at each iteration, rather than each observation being created individually and then combined at the end. A polarization vector catalog is then created using the Stokes I , Q , and U maps. The data were reduced using a pixel size of $8''$ with a $14''$ beam. The final Stokes I , Q , and U maps were flux calibrated, in units of millijansky per beam, using a flux calibration factor (FCF) for $850\ \mu\text{m}$ of $748\ \text{Jy beam}^{-1}\ \text{pW}^{-1}$, and in units of millijansky per square arcsec using a FCF of $2.93\ \text{Jy arcsec}^{-2}\ \text{pW}^{-1}$.¹⁹

The final polarization values in the vector catalog are debiased using the Stokes Q and U variances to remove the statistical bias in regions of low S/N (Wardle & Kronberg 1974).

The values for the debiased polarization, P , were calculated from

$$P = \frac{1}{I} \sqrt{Q^2 + U^2 - \frac{1}{2}(\delta Q^2 + \delta U^2)}, \quad (2)$$

where I , Q , and U are the Stokes parameters, and δQ and δU are the uncertainties for Stokes Q and U . The uncertainty, δP , of

¹⁷ Canadian Astronomy Data Centre: <https://www.cadc-ccda.hia-ihp.nrc-cnrc.gc.ca/en/>.

¹⁸ <http://starlink.eao.hawaii.edu/docs/sc22.pdf>

¹⁹ These conversions were done using the CALIBRATE-SCUBA-2-DATA recipe under the PICARD package in Starlink.

¹⁶ See also presentation no. 5, e-proceedings, of “From Stars to Galaxies II”: <http://cosmicorigins.space/fstgii>.

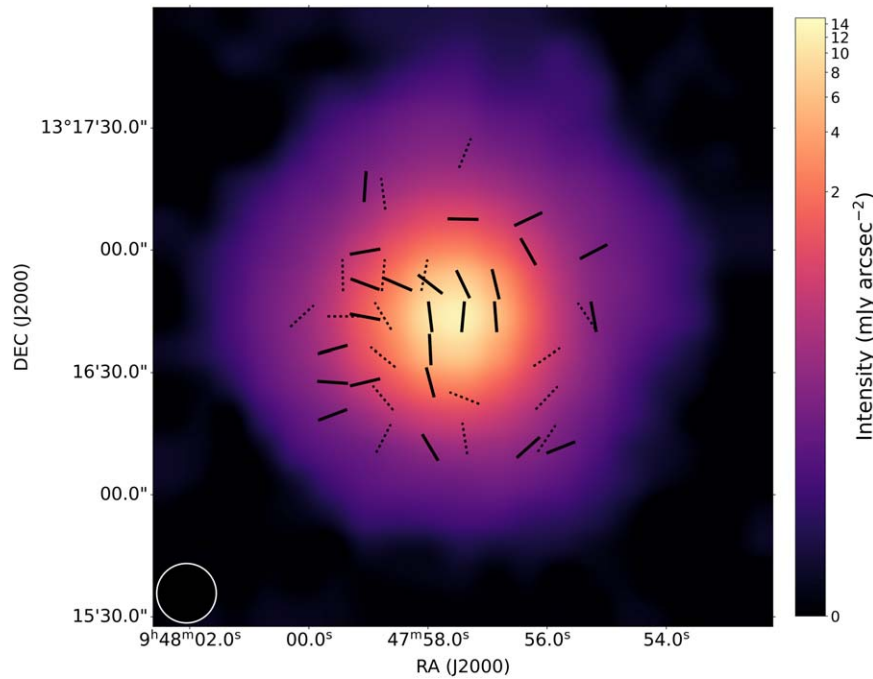


Figure 1. The SCUPOL polarization vectors (Matthews et al. 2009) with $I/\delta_I > 0$ and $P/\delta_P > 2$ are shown as black dotted vectors (binned to a $10''$ grid), with our POL-2 polarization vectors in solid black (on an $8''$ grid) with $I/\delta_I > 20$ and $P/\delta_P > 2.5$. The POL-2 data have better sensitivity than the SCUPOL data, with approximately 50% more vectors at the same S/N cut. The color background shows the POL-2 Stokes I component, with the SCUBA-2/POL-2 $850 \mu\text{m}$ beam size shown in the bottom left. All beam sizes quoted in this paper are in terms of FWHM.

polarization was obtained using

$$\delta P = \sqrt{\frac{(Q^2 \delta Q^2 + U^2 \delta U^2)}{I^2(Q^2 + U^2)} + \frac{\delta I^2(Q^2 + U^2)}{I^4}}, \quad (3)$$

with δI being the uncertainty for the Stokes I total intensity.

The polarization position angles, θ , increasing from north to east in the sky projection, were measured using the relation

$$\theta = \frac{1}{2} \tan^{-1} \frac{U}{Q}. \quad (4)$$

The corresponding uncertainties in θ were calculated using

$$\delta\theta = \frac{1}{2} \frac{\sqrt{Q^2 \delta U^2 + U^2 \delta Q^2}}{(Q^2 + U^2)} \times \frac{180^\circ}{\pi}. \quad (5)$$

Vectors were then selected using S/N cuts of $I > 20\delta I$ and $P > 2.5\delta P$. The selection criteria were chosen as a compromise between high-S/N constraints and maintaining a significant number of polarization vectors. The cut in polarization is roughly equal to an uncertainty in the position angle of $\delta\theta = 11.5^\circ$ (Naghizadeh-Khouei & Clarke 1993), which is quite reasonable. The S/N constraints are common throughout studies using SCUBA-2/POL-2 data (e.g., Kwon et al. 2018; Liu et al. 2019).

The earlier observations of IRC+10216 with SCUPOL (Matthews et al. 2009) are of lower S/N, with cuts of $I > 0$ and $P > 2\delta P$. We show the SCUPOL polarization vectors plotted with our POL-2 vectors in Figure 1. When applying a similar S/N cut to the SCUPOL vectors as our own, we have $\sim 50\%$ more vectors with POL-2, increasing from 15 to 22 vectors. We can also compare the vectors that spatially match. There are only seven vector pairs that spatially match within $8''$, which we have chosen due to our vector catalog being binned to $8''$. While the polarization amount is generally mutually consistent,

the polarization angles vary significantly, with only three vectors agreeing well within the position angle uncertainties for moderate-S/N data (Naghizadeh-Khouei & Clarke 1993). We note that SCUPOL was a different polarimeter and observed in a different mode than POL-2, which is a significant upgrade in sensitivity and ability to deal with atmospheric variations. As such, we do not expect perfect agreement, but the POL-2 data are of higher quality.

Figure 2 shows the azimuthally averaged variation of intensities of different wavelength emissions with the offset from IRC+10216. The beam sizes corresponding to each observation are also indicated in the plots. The variation of $53 \mu\text{m}$ intensity with radius is clearly different from that of $850 \mu\text{m}$, while both are decreasing with offset. However, a similarity in the intensity variations of 154 and $850 \mu\text{m}$ can be noticed in the right panel of the figure. The data for the 53 and $154 \mu\text{m}$ traces are taken from Andersson et al. (2022).

3. Analysis

Both at small (e.g., De Beck et al. 2012) and large (e.g., Mauron & Huggins 1999) scales, the overall density of the shell is well described by a $n \propto r^{-2}$ density, out to the astrosphere (Ladjal et al. 2010; Sahai & Chronopoulos 2010). Modeling using both DUSTY (Ivezić et al. 1999), as in Ivezić & Elitzur (1996a) and Andersson et al. (2022), and MCMAX (Min et al. 2009), as in De Beck et al. (2012), yield good agreement between the emitted spectra and a monotonously decreasing temperature distribution in the envelope (e.g., Ivezić & Elitzur 1996b; De Beck et al. 2012; Andersson et al. 2022). The emission at both FIR and submillimeter wavelengths are optically thin (Ivezić & Elitzur 1996a; Andersson et al. 2022, Table 4 of the latter), and for the radial offsets from the star considered here, the dust temperature is low enough ($\lesssim 200$ K) that all our observed wavelengths are well into the Rayleigh-

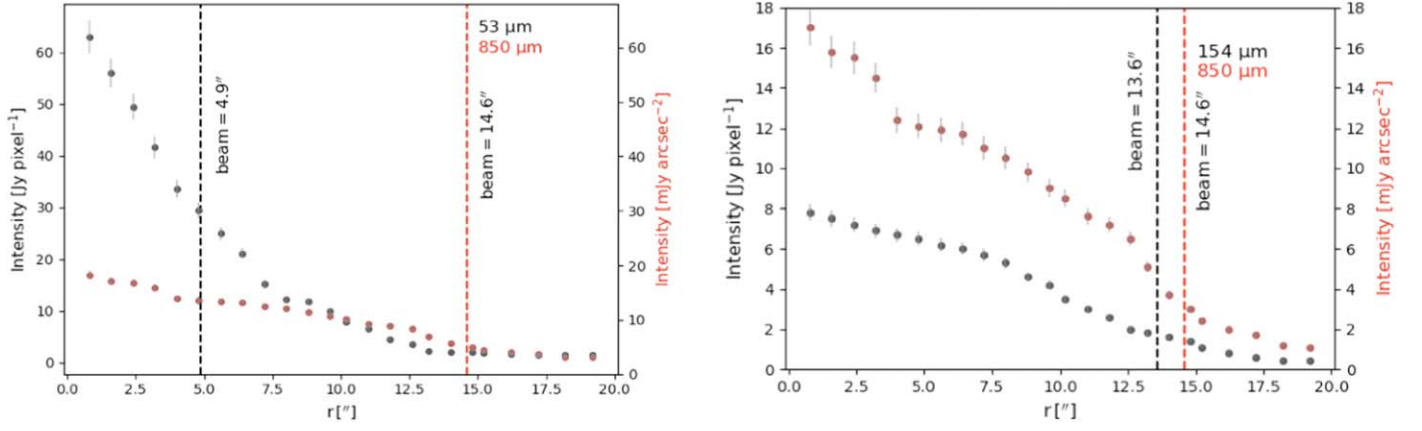


Figure 2. Left: The variation of Stokes I intensity with the projected radius of IRC+10216 in 53 and 850 μm wavelengths is shown. (These are azimuthally averaged fluxes around the star. Shells of $2''$ width were drawn around the central star and the average flux was extracted in those shells.) Right: The same plot, but for 154 and 850 μm wavelengths. Vertical dashed lines indicate the beam sizes in respective wavelengths.

Jeans limit. Therefore, the Stokes I emission from the shell, for all wavelengths considered, is dominated by the density profile in the CSE.

3.1. Radial Coordinate Polarization

To better study the radial polarization in IRC+10216, we use the radial Stokes parameters Q_r and U_r , as defined in Equation (6), where the reference frame is rotated by the polar angle at each point with respect to the star's location:

$$Q_r = +Q \cos 2\xi + U \sin 2\xi, \quad U_r = -Q \sin 2\xi + U \cos 2\xi, \quad (6)$$

where $\xi = \arctan \frac{x-x_0}{y-y_0}$ is the polar angle of a given pixel coordinate position (x, y) (corresponding to equatorial coordinates) and (x_0, y_0) is the location of the star. Because of the moderate decl. of IRC+10216 ($\sim 13.25^\circ$) we have omitted the $\cos(\delta)$ factor for the R.A. distance in the numerator.

Positive Q_r shows radial polarization, while negative Q_r indicates tangential polarization. U_r represents polarization with an angle of $\pm 45^\circ$ from the radial direction. Therefore, zero U_r indicates purely radial or tangential polarization.

We take thin annuli ($\sim 2''$ in HAWC+ and $\sim 14''$ in JCMT observations) around the star and find the averaged Q_r and U_r in each annulus to identify the radial profile of Q_r and U_r . Following that, we determine

$$\theta_r = 0.5 \times \arctan \left(\frac{\langle U_r \rangle}{\langle Q_r \rangle} \right), \quad (7)$$

as defined by Tahani et al. (2023) and shown in Figure 3 for the HAWC+ 53 μm (upper left panel), HAWC+ 154 μm (upper right panel), and the JCMT POL-2 850 μm observations (lower panel). The data have the same constraints of $S/N(I) > 20$ and $S/N(P) > 2.5$. Allowing for 5% uncertainty, a point with $\cos \theta_r > 0.95$ (including their error bar) represents radial polarization at that radius. This choice is clearly somewhat arbitrary but, as can be seen from Figure 3, provides a reasonable separation between systematically radial and nonradial polarization. The HAWC+ 53 μm observations show clear radial polarization between $6''$ and $45''$, while the JCMT observations do not indicate a clear radial polarization.

The HAWC+ 154 μm observations show radial polarization only from $5''$ to $28''$.

The blue “x” markers in Figure 3 show the number of pixels with polarization measurements included for each radial bin. Comparing the uncertainties indicated for the $\cos(\theta_r)$ values with the variation in the number of points per bin shows that the dominant source for the larger uncertainties is dispersion within each sample, rather than localized higher measurement errors.

3.2. CN Zeeman

Duthu et al. (2017) observed the Zeeman effect in the IRC+10216 CSE, using the CN ($J=1-0$) line at 113 GHz with the IRAM 30 m telescope. They detected the line-of-sight magnetic field in five locations around the central star (plus one upper limit), with radial offsets ranging from $18''$ to $27''$. Because of the varying distances from the star, they—and we—scale the observations to a common distance from the star to allow comparisons with models. They normalized their measurements to a common distance using a r^{-1} dependence, based on Vlemmings (2012). As shown by Figure 4, a coherent variation of the line-of-sight B field is indicated by these data. We used this r^{-1} scaling, as well as a r^{-3} scaling, appropriate for a dipole field, and fit the resulting values to an azimuthal cosine function:

$$B_{\text{LOS}} = a \cdot \cos(\Theta - \Theta_0). \quad (8)$$

With the limited number of data points and marginal S/N, these fits are not conclusive, but provide an indication of the magnetic field structure in the CSE, especially the orientation of a possible dipole field orientation. Figure 4 shows the best-fit cosine functions (weighted, in solid lines, and unweighted, in dashed lines) of the Duthu et al. (2017) data for both scalings (r^{-3} in blue and r^{-1} in black). We show both types of fits, since we scaled also the uncertainties in the B field by the two radial scalings. In the fits, we have set the value at $(-18, -10)$ —an upper limit in Duthu et al. (2017)—to zero and assigned the upper limit as the uncertainty (indicated in Figure 4 by wedges showing the upper limit and open symbols for the value used in the fits). Consistent results are found if the point is simply omitted. The various fits give mutually consistent results. In all cases, a pole orientation around 90° – 125° east of north is

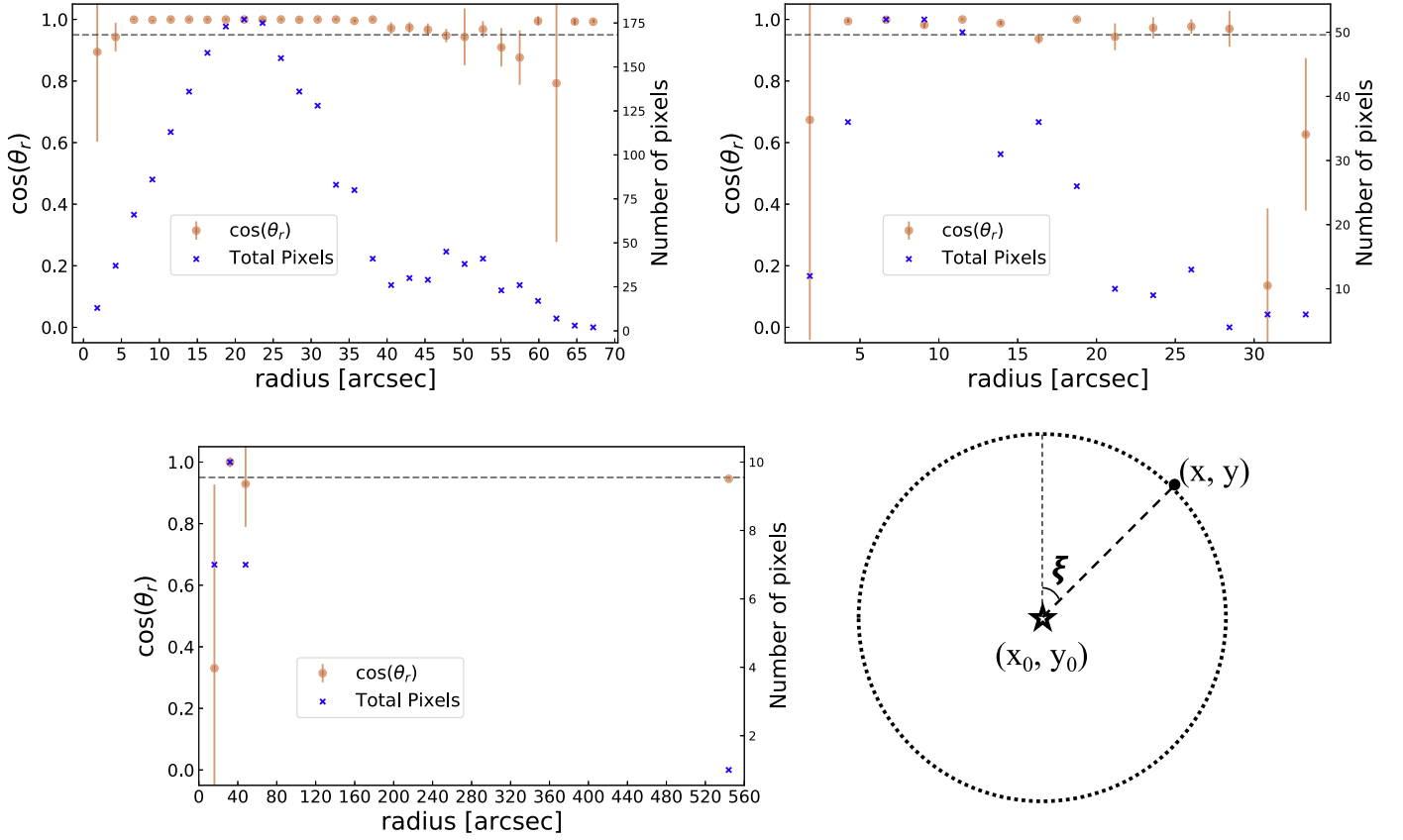


Figure 3. Radial polarization with $S/N(I) > 20$ and $S/N(P) > 2.5$. The x - and y -axes represent the radial profile of $\cos \theta_r$ as described in Equation (7) and the radius from the center of the star. The dashed horizontal line shows $\cos \theta_r = 0.95$, with points above this line (including their error bars) representing radial polarization (allowing for 5% uncertainty; see Tahani et al. 2023 for more detail). The blue dots illustrate the number of pixels (satisfying the S/N cut) in each annulus. Upper left: HAWC+ $53 \mu\text{m}$ observations. Upper right: JCMT POL-2 observations. Lower left: JCMT POL-2 observations. Lower right: a cartoon illustrating the radial polarization frame (see Equation (6)).

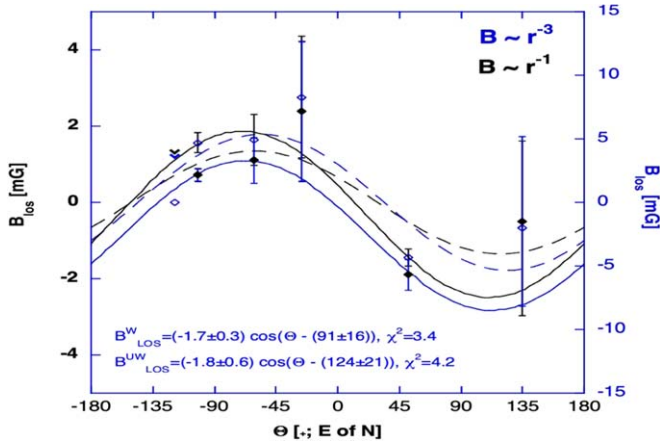


Figure 4. The line-of-sight magnetic field strength, based on the CN ($J = 1-0$) Zeeman observations of Duthu et al. (2017), scaled to a common radial distance from the central star using an r^{-3} scaling (blue open symbols and curves, right axis) and using an r^{-1} scaling (black filled symbols and curves, left axis). The weighted (W; solid lines) and unweighted (UW; dashed lines) fits yield consistent results, both in amplitude and phase (see text for details).

found, albeit with significant uncertainties. For the r^{-1} scaling, the weighted and unweighted fits, we find pole orientations of $113^\circ \pm 17^\circ$ and $119^\circ \pm 21^\circ$, respectively. For the r^{-3} scaling, the weighted and unweighted fits yield pole orientations of $91^\circ \pm 16^\circ$ and $124^\circ \pm 21^\circ$, respectively.

3.3. Dipole Modeling

Given the clearly nonradial polarization pattern in the $850 \mu\text{m}$ data, contrasting with the FIR HAWC+ 53 and $154 \mu\text{m}$ results, an alternative polarization geometry is required—unless the geometry is inherently random. However, a truly random orientation of the grains and/or geometry would produce a zero polarization. Hence, we need an ordered structure in the CSE that could allow grain alignment and produce the nonradial polarization pattern observed. Based on the results of Szymczak et al. (2001) and Vlemmings et al. (2005), the fits to the Zeeman data discussed above, and the simplicity of geometry (lowest-order terms of a spherical harmonic expansion), we chose this to be a projected dipole field. This implies a *magnetic* dipole, but does not at this point require it.

We therefore compared the observed $850 \mu\text{m}$ polarization pattern to a simple model of a projected magnetic dipole of the form described in the Appendix. Because of the simplifying assumptions in our model, we only use the position angles, but not the amount of polarization, in our fitting. We generated a family of models with varying rotation angles Θ , where Θ is the rotation of the dipole model (E -vectors) in the plane of sky (POS). We took the CSE to be the central area where $I/\delta_I > 10$ (though we maintained our $I/\delta_I > 20$ cut on polarization vectors in this area), which was a region with diameter of $\approx 104''$. We generated the dipole on a 104×104 grid and set the spacing to $1''$. We sought a maximum-likelihood estimate

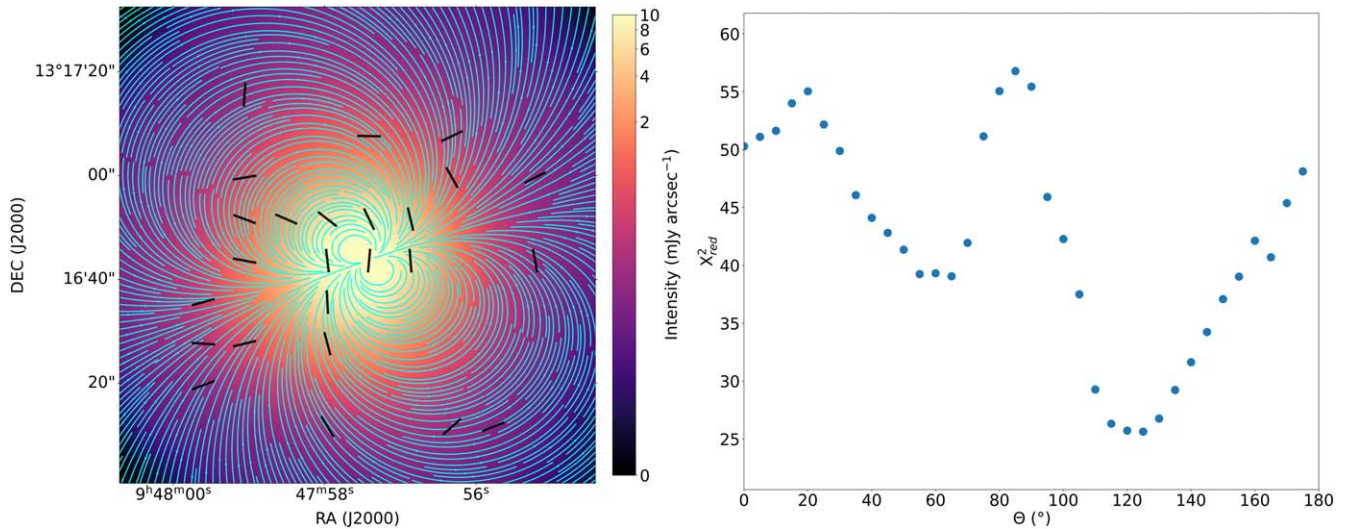


Figure 5. Left: The $850\ \mu\text{m}$ dust emission map is shown with the POL-2 $850\ \mu\text{m}$ polarization vectors ($I > 20\delta_p$ and $p > 2.5\delta_p$) plotted in black over the best-fit dipole morphology shown by the cyan stream-plot (the orientation of the field lines represent the polarization “ E -vectors”). The image is zoomed in to show just the envelope. Right: A plot of the reduced χ^2_{red} value, which is found using Equation (9), as it varies with the different field rotations Θ . A minimum can be seen around $\Theta = 125^\circ$ (E -vectors) with an uncertainty of $\sim 15^\circ$.

(MLE; Bevington & Robinson 1992) of the model rotation angle, by performing a χ^2_{red} minimization of the model fits to the polarization position angle data. We used the χ^2_{red} normalization in the least-squares MLE since this provides an indication of the absolute goodness of the model fits. Because the uncertainties for polarization data (amount p , and position angle θ) for marginal S/N are not Gaussian, care has to be taken in such minimization. We used the analysis of such non-Gaussian position angle uncertainty distributions by Naghizadeh-Khouei & Clarke (1993, specifically their Equations (3) and (4)) to assign the weights in the χ^2_{red} modeling of the position angles. With our limited selection of only vectors with $p > 2.5\delta_p$ this should be a minor concern, but we include the factor of 1.2 in Equation (9).

In the fitting, we fix the center of the dipole model at the center of the observed map. We calculated models on a fixed rectangular grid, over a POS rotation Θ of 0° – 180° , in spacings of 5° . For each case we find the closest model vector to each observed polarization vector. We then calculate a goodness-of-fit parameter (reduced χ^2_{red} ; Bevington & Robinson 1992; but see also Andrae et al. 2010) for that rotation Θ :

$$\chi^2_{\text{red}} = \frac{\sum_{i=1}^n \frac{(\theta_{\text{obs}} - \theta_{\text{model}})^2}{(1.2\delta_\theta)^2}}{N - N_c}, \quad (9)$$

where N is the number of data points fitted (25 POL-2 vectors passed our S/N threshold), N_c is the number of constraints in the model (here just one: Θ), δ_θ is the uncertainty in polarization position angle (see Equation (5)), and θ_{obs} and θ_{model} are observed polarization position angle (see Equation (4)) and polarization position angle from the model, respectively. The best-fit model is overlaid on the observational data in the left-hand panel of Figure 5. The resulting reduced χ^2_{red} plot is shown in the right-hand panel of Figure 5. We find a clear minimum χ^2_{red} of ~ 25.6 when the dipole is rotated to $\Theta_E = 125^\circ$ east of north (or -55° with the normal POL-2 notation). The average measurement uncertainty for the position angles is 11.5° with a standard deviation of 6.5° .

The rotation angle is well constrained, with a fitting uncertainty of $\sim 15^\circ$.

The minimum value of reduced $\chi^2_{\text{red}} \sim 26$ in our analysis indicates that this is either overall not a good fit, or that the model is not a complete description of the data. Given the clear minimum in the χ^2_{red} , we explore its significance with two simple tests (see Andrae et al. 2010). Figure 6 (left) shows the distribution of residuals between the observed and modeled position angles at the χ^2_{red} minimum. While broad, the residuals show a peaked distribution centered on zero (within the uncertainty). The normalized residuals also show a clear Gaussian distribution, centered at zero, albeit with $\sigma^2 \gg 1$. Additionally, we performed a jack-knife test (Lupton 1993; Andrae et al. 2010), where we omitted each data point, in turn, and repeated the χ^2_{red} minimization. The resulting variation in $\chi^2_{\text{red}}(\Theta)$ is shown in the right-hand panel of Figure 6. The general shape of the fit results, and location of the minimum, are consistent for all data point exclusions. These results point to a dipole as being a meaningful part of the true, underlying, magnetic field geometry. More and higher S/N data, as well as a full radiative-transfer model treatment, are required to conclusively address this question.

With the reasonable fit to the $850\ \mu\text{m}$ data, and since the $154\ \mu\text{m}$ SOFIA/HAWC+ data at offsets beyond $\sim 30''$ from the central star show significant deviations from a fully radial polarization pattern, we applied the model also to the $154\ \mu\text{m}$ SOFIA/HAWC+ observations. If we combine a “mono-pole” (radial) geometry inside $30''$ with a dipole model at larger radii for the $154\ \mu\text{m}$ observations, the vectors in the northeastern quadrant can be better fit than by a radial geometry alone. Even so, the overall reduced χ^2 for the fit with only a mono-pole component is lower than for the combined fit.

3.4. Comparison of Polarization Properties in Different Wavelengths

The clear differences in the polarization geometry between the 53 and $850\ \mu\text{m}$ data make it worthwhile to directly compare the polarization at several wavelengths. Figure 7 compares the

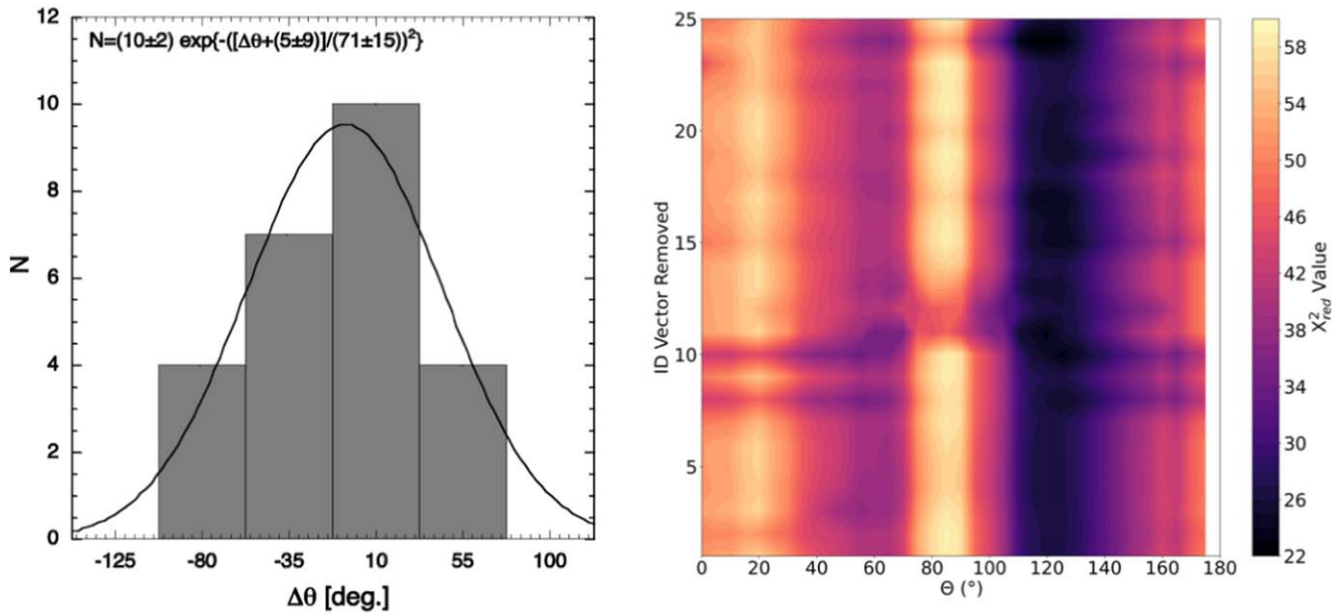


Figure 6. To test the validity of the χ^2 minimization, noting that the reduced χ^2 never approaches zero, we follow Andrae et al. (2010). Left: the residuals for the best-fit solution yield a peaked distribution. Right: recalculating the χ^2 minimization while eliminating each of the data points, in turn, shows a consistent χ^2 minimum. The ordinate shows the eliminated data point (arbitrarily numbered).

polarization geometry for the 53, 154, and 850 μm data. The 154 μm does show a somewhat intermediary geometry, possibly indicating a transition from the radial polarization seen at 53 μm to the “dipole-like” structure seen at 850 μm . We note, however, that while the beam sizes at 154 and 850 μm are comparable, they are significantly larger than that for 53 μm , so the comparison is not fully straightforward.

Figure 8 shows the polarization fractions at 53, 154, and 850 μm , as functions of the total intensities. A similar drop from high polarization and low intensities at larger radii to low polarization and high intensities near the star can clearly be seen for all wavelengths. Fitting single-component power laws, the drop is steeper for 850 μm , with a slope (exponent of a power law) of -0.89 ± 0.04 . Shallower, single-slope relations are found for 154 μm (slope = -0.41 ± 0.09) and for 53 μm (slope = -0.31). As is clear from Figure 8, a single-component power law may, however, not be adequate, especially for the 53 μm data. A two-power-law fit to the 53 μm data yields an initial slope consistent with that for the 850 μm data (slope = -0.85 ± 0.06), with a slope of -0.45 ± 0.05 at higher intensities, slightly offset to higher polarization fractions. The 154 μm polarization shows an indication of a similar offset/second slope at the highest intensities in that band ($I \geq 0.2 \text{ Jy arcsec}^{-2}$). This potential second distribution is most strongly indicated by the fact that if the 154 μm data were fitted to only intensities less than $\sim 0.1 \text{ Jy arcsec}^{-2}$, a significantly steeper power law would have resulted (slope = -0.71 ± 0.02). The “jump” in the 53 μm polarization occurs at $\sim 3 \text{ Jy arcsec}^{-2}$. As Figure 2 shows, the two intensities occur at a similar radial distance from the central star of $r \approx 12''.5$. We note that, at this radius, the Stokes I intensity for the 850 μm emission is $\sim 6.5 \text{ mJy arcsec}^{-2}$ and therefore well beyond the current polarization sensitivity. Hence, the polarization fractions in each band vary in similar manners, with a steeper slope at large distances in the CSE and shallower slopes inside about $12''.5$. This may indicate a change in alignment mechanism within the shell, or a reduction in the alignment efficiency (including

disalignment effects) closer to the star. While the higher gas density and dust temperature closer to the central star would both nominally imply larger collisional and radiative disalignment (see Draine & Lazarian 1998), we would not expect them, by themselves, to be able to explain the discrete change in slope of the polarization. Both the radiation field and gas density in CSEs are expected to be continuous and vary smoothly with radius. Although significant, small-scale structure is known to exist in the CSE (e.g., Maunon & Huggins 1999; Leão et al. 2006; Ladjal et al. 2010), the general r^{-2} radial density dependence will still dominate the radial density profile. Hence, the observed discrete changes in polarization efficiency likely require a more qualitative change in the grain alignment, such as a different mechanism.

3.5. Line Polarization

As noted above, G-K polarization (Goldreich & Kylafis 1981, 1982) has been observed in several submillimeter-wave lines in the envelope of IRC+10216 (Girart et al. 2012). The authors mapped the linear polarization from the lines of CO ($J=3-2$) at $\nu=345.796 \text{ GHz}$, SiS ($J=19-18$) at $\nu=344.779 \text{ GHz}$, and CS 7-6 at $\nu=342.883 \text{ GHz}$. These lines are all located at wavelengths with transmissions above 95% of the peak transmission of the SCUBA-2 850 μm filter (Cookson et al. 2018). The SMA primary beam (6 m antennae) at 850 μm is about $36''$, and Girart et al. (2012) achieved a synthesized beam of $2''.6 \times 1''.6$. Also, as shown by Girart et al. (2006), the SMA filters out emission that arises from structures larger than about $10''$, so the two data sets are not trivial to compare in a quantitative way. However, if we use the CO data from Girart et al. (2012) and the conversion factors given in Drabek et al. (2012), we can estimate the possible G-K contamination in our observations. Using the Girart et al. (2012) measurement of the Stokes Q parameter, we find a peak line brightness temperature of 2 K and a width of 20 km s^{-1} . If the JCMT conversion factor is valid also for the Stokes Q parameter, we find a polarized intensity on the order of

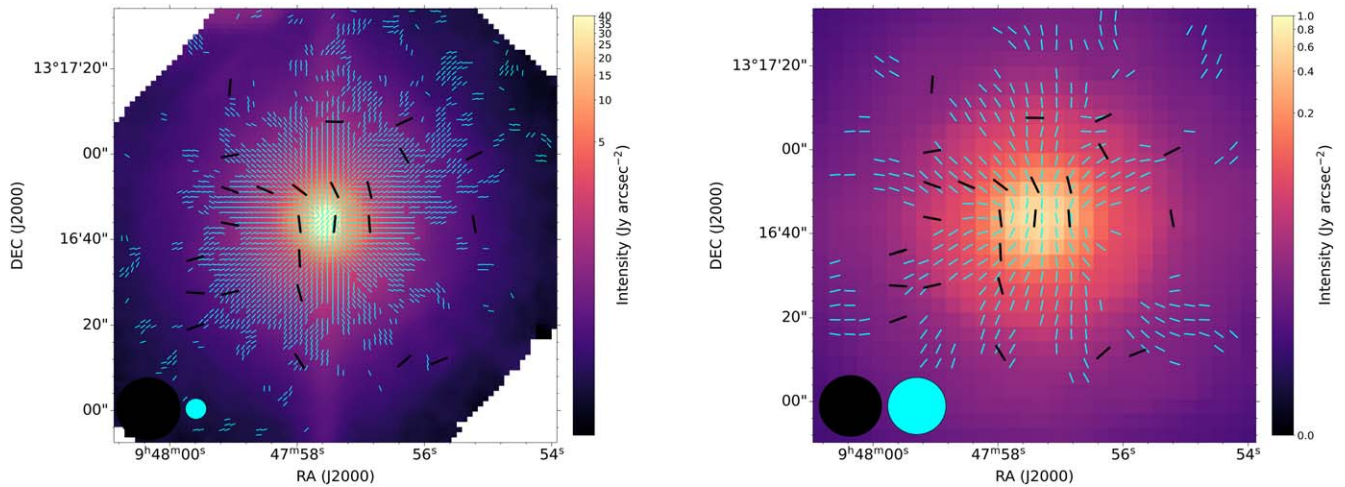


Figure 7. Left: The SOFIA/HAWC+ $53\ \mu\text{m}$ polarization vectors in cyan in the envelope of IRC+10216 with JCMT/POL-2 $850\ \mu\text{m}$ polarization vectors overlaid in black. Background image is the $53\ \mu\text{m}$ emission. Right: The JCMT/POL-2 $850\ \mu\text{m}$ data in black overlaid on SOFIA/HAWC+ $154\ \mu\text{m}$ emission with polarization vectors in cyan. Because of the large beam sizes, relative to the offset from the CSE center, the $850\ \mu\text{m}$ data may be prone to significant beam-averaging and not show the true polarization. In this figure, we show the oversampled maps of the HAWC+ data to emphasize the differences in polarization geometry. Beam sizes are shown in the lower-left corner.

$30\ \text{mJy beam}^{-1}$, which would contribute a significant signal in our polarized intensity, assuming the spatial filtering does not strongly affect the comparison.

However, if we compare the polarization geometry between our observations (SOFIA/HAWC+ and JCMT/POL-2) with those of Girart et al. (2012), the picture becomes more complicated. As Figure 9 shows, the latter only detects emission in the very inner part of the CSE and our field of view, where we might expect beam-averaging effects in the JCMT/POL-2 data. Nonetheless, none of the CO, SiS, or CS line-emission data show polarization geometries that are consistent with those seen in the continuum, either at 53 or $850\ \mu\text{m}$. In addition, the position angle of the CS ($J=7-6$) emission ($\text{PA} \sim 48^\circ$) is close to perpendicular to those for CO ($J=3-2$) emission ($\text{PA} \sim 155^\circ-170^\circ$) and SiS ($J=19-18$) emission ($\text{PA} \sim 139^\circ$), and the different line polarization components would therefore offset each other within the broad SCUBA-2 bandpass filter (and larger beam).

3.6. Grain Charging

Charged grains can interact with a surrounding magnetic field, even for diamagnetic grains. As we discuss below (Section 5.3), a recently formulated grain alignment mechanism (E-RAT; Lazarian 2020) predicts that grains not susceptible to paramagnetic interactions can achieve efficient alignment with the magnetic field, if they are charged and possess a relative motion to the field.

For dense AGB star CSEs the photoionization of the gas, and charging of the dust, is expected to be strongest in the outer envelope and originate from the UV light in the diffuse interstellar field (because of the cool effective temperature of the central star, very little UV flux is expected from its photosphere). Since we do not have any direct observational tracer of the grain charging, we used the gas electron density calculated in the detailed chemical modeling of IRC+10216 by Cordiner & Millar (2009) and Li et al. (2014) as a proxy for the grain charging as a function of radius. Figure 10 shows a comparison of the polarization fraction to the electron density.

For interstellar conditions, where grain–electron collisions are an important aspect of the grain charge balance

(Weingartner & Draine 2001), we would expect the grain charge to be proportional to $1/n(e)$. However, the conditions in the CSE (low fractional ionization, fully molecular hydrogen, high flow speed, and steep density gradient, etc.) may mean that the collisional effects are negligible, and the grain charge will be determined by photoelectric emission balanced by the electrostatic potential of the grain, and hence be dependent on the opacity to the interstellar radiation field but not involve the $1/n(e)$ factor, as implied by the semi-empirical correlation seen in Figure 10. Detailed modeling, applicable to the conditions of the CSE (beyond the scope of this paper), will be needed to fully address this issue.

While for small grains the electric moment can originate as part of grain structure (Draine & Lazarian 1998), for the large grains indicated in the IRC+10216 CSE (e.g., Groenewegen 1997) grain charging is likely required (A. Lazarian 2022, private communications). Since the electric dipole moment of a grain depends on the total charge on the grain (see Weingartner 2006; Lazarian 2020), we use the space density of electrons as our proxy for grain charging and electric alignment. The blue dashed line in the outer envelope corresponds to electrons released by photoionization, while the red dashed curve corresponds to electrons due to cosmic-ray ionization. Ivlev et al. (2015) have argued that grain charging by cosmic rays in the inner envelope, which is similar in gas parameters to their region “ \mathcal{I} ,” should be inefficient.

4. Results

Our FIR, especially the $53\ \mu\text{m}$, and optical polarization data (Andersson et al. 2022; B-G. Andersson et al. 2024, in preparation) indicate grain alignment with the long axis in the radial direction away from the central star, supporting a second-order radiative grain alignment mechanism (Hoang & Lazarian 2009). We stress that, as we argued in the former paper (Andersson et al. 2022), the radial dependence of the FIR polarization does not support a mechanical (gas-dust drift) alignment mechanism (e.g., Gold 1952) as the primary driver. The JCMT/POL-2 $850\ \mu\text{m}$ data presented here do not, however, show this simple radial pattern, even in the inner part of the CSE.

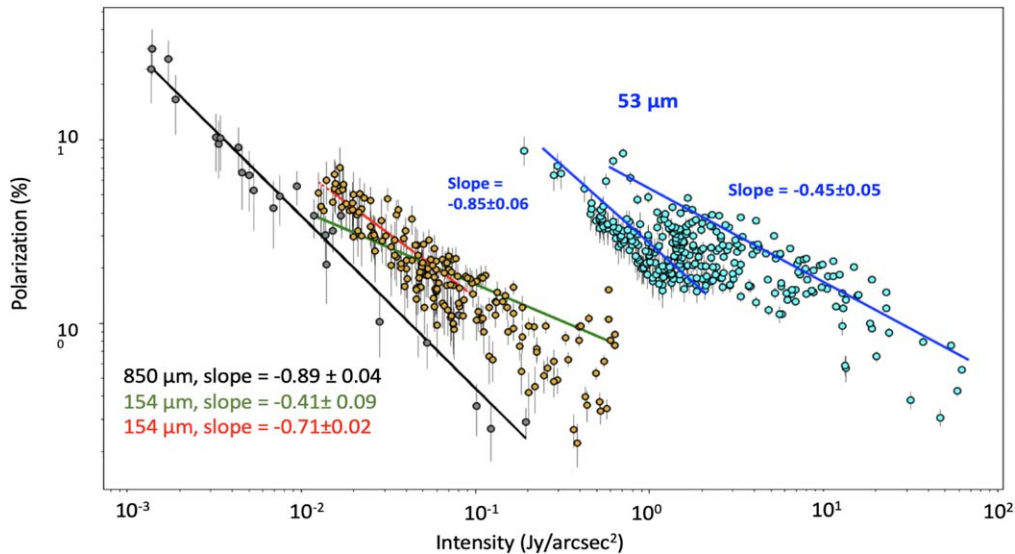


Figure 8. The polarization fraction for the 53, 154, and 850 μm polarization is plotted against the Stokes I intensities at each wavelength. For the 850 μm data, a single well-defined power law is apparent. The 53 μm is well fit by a two-component distribution with a steeper slope at small fluxes (similar to the 850 μm one) followed by a shallower slope, offset to somewhat higher values at the intersection. The 154 μm falls in between the two, with a hint of an offset, seen in the 53 μm data, at the high end of the 154 μm intensity distribution. If the 154 μm data are fit to only intensities less than 0.1 Jy arcsec^{-2} , an exponent consistent with that for the steep part of the 53 μm and the 850 μm data is found (see text for details). All data have been debiased.

The analysis utilizing the radial coordinate polarization (Section 3.1) shows a distinct difference between the FIR (SOFIA/HAWC+) and submillimeter-wave (SCUBA-2/POL-2) data. Again, for the FIR, the $\cos \theta_r > 0.95$ (for all 53 μm data and inside $r \approx 32''$ for the 154 μm data) indicate a clear radial polarization pattern (Figure 3, upper panels). While of lower S/N, and at somewhat different scales, the plots indicate neither a radial nor a tangential pattern in the submillimeter-wave data in Figure 3 (lower panel).

Using the Zeeman measurement results of Duthu et al. (2017), we find a periodic variation in the line-of-sight magnetic field around the star, with the pole of the possible underlying dipole field oriented at around 90° – 125° , albeit with relatively large uncertainties. We therefore assume a multipole expansion of a potential magnetic field and apply a simple dipole model fit to the 850 μm data.

As Figure 5 shows, there is a clear χ^2 minimum found for a rotation angle of $\Theta_E = 125^\circ$. The modeling is done for E -vectors. The relationship to a possible magnetic dipole field axis is ambiguous, depending on the alignment mechanism, even if involving magnetic fields (see Section 5.3). The polarization symmetry axis is close to that of the Zeeman results and of the torus seen by Jeffers et al. (2014).

While our simple model uses only a *projected* dipole term for a possible magnetic field and does not fully account for all measured orientations of the polarization field, it is clear that the FIR and submillimeter-wave data do not show the same (dominant) polarization patterns.

Comparing to the line polarimetry by Girart et al. (2012) shows that, while significant, G-K polarization of spectral lines within the SCUBA-2 passband is unlikely to explain the observed 850 μm continuum polarization (Section 3.5).

As shown by Figure 8, the slope (power-law exponent) of the fractional polarization as a function of total intensity is nominally steeper for the 850 μm polarization than for the 53 μm or 154 μm ones. Allowing a two-power-law fit to the 53 (and 154) μm data, however, shows that at small respective intensities all three share a common slope of approximately

-0.85 . The second power-law parameters are only measurable for the 53 μm data, yielding a slope of -0.45 , with an offset to higher polarization fractions for a given intensity, with the transition between the two at $\sim 3 \text{ Jy arcsec}^{-2}$. The 154 μm polarization shows an indication of a similar change at $I \approx 0.2 \text{ Jy arcsec}^{-2}$. These intensities both occur at a radial offset from the star of $\sim 12''$ (Figure 2). While this is comparable to the beam size at 154 μm , it is significantly bigger than the 53 μm beam.

Figure 10 shows a correlation between grain charging and alignment in the outer envelope of IRC+10216 beyond an offset radius of $\sim 20''$.

5. Discussion

As shown by our polarization maps and the azimuthally averaged radial polarization plots, the 850 μm polarization is dominated by neither a radial nor an azimuthal pattern. The small number and asymmetric distribution of the JCMT polarization detections make the difference between 53 and 850 μm data difficult to interpret conclusively. However, the nonradial polarization in the latter data set does require a different polarization mechanism than we have proposed for the FIR data.

For the inner part of the CSE, the large beam size ($14''$), relative to the offset from the center of the CSE, means that the JCMT data is prone to (possibly severe) beam-averaging effects. However, as can be seen from Figure 7, the beam-averaged polarization even inside $\sim 20''$ of the central star is often azimuthal (or, at least, nonradial) in orientation. By symmetry, a beam-averaged radial pattern would remain radial, and therefore it is unlikely that the beam size can explain this dichotomy between the FIR and submillimeter-wave polarization for dust at a (three-dimensional) radial distance from the central star comparable to the projected distance of these measurements.

If the more efficient 850 μm polarization is due to the dust, then it indicates that some of the grains have acquired efficient

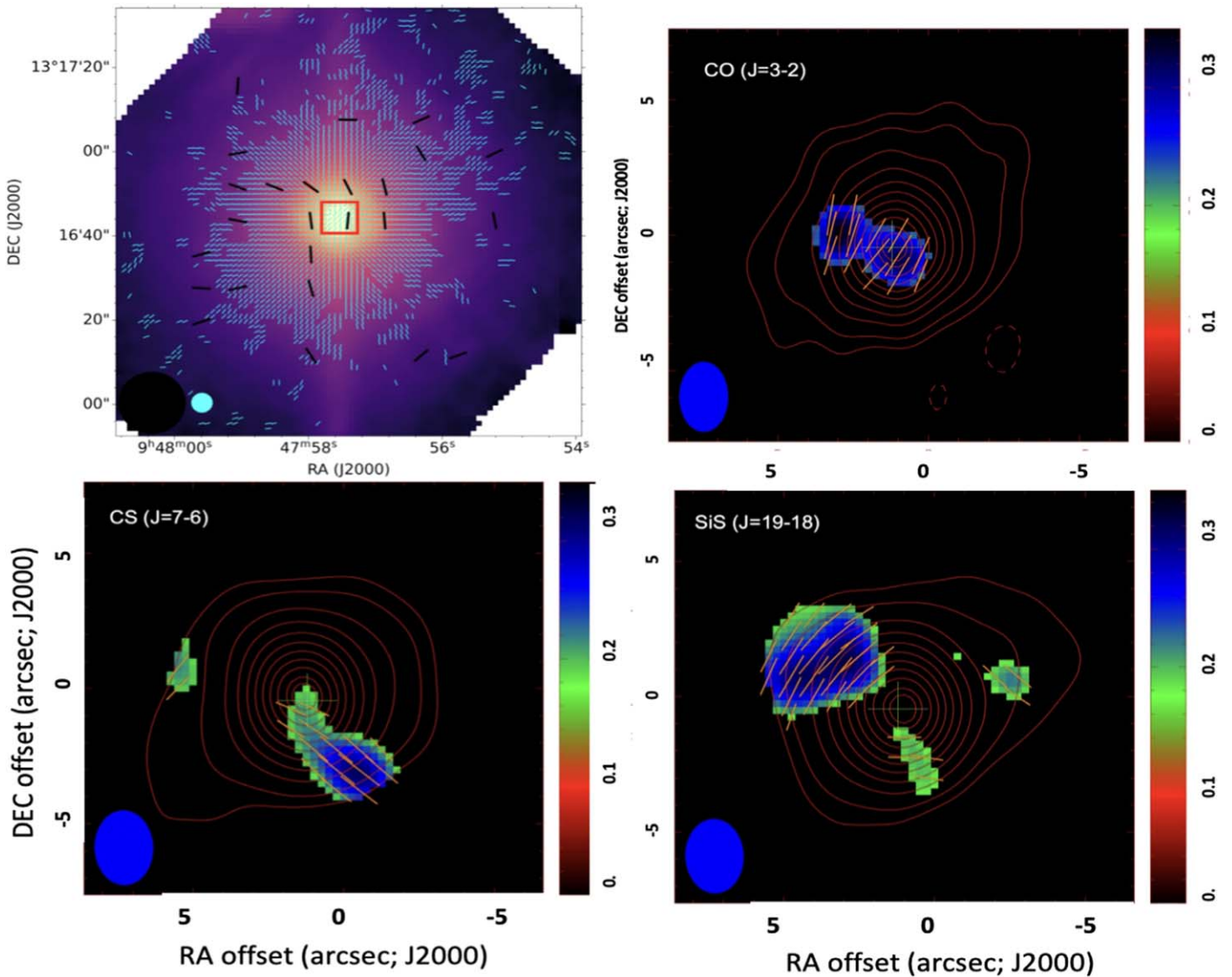


Figure 9. Comparison between the (upper left) JCMT/POL-2 $850\ \mu\text{m}$ (black vectors) and SOFIA/HAWC+ $53\ \mu\text{m}$ (cyan vectors) polarization with the line polarization observation by Girart et al. (2012, reproduced with permission). The red square in the upper-left map shows the approximate extent of the three sub-figures from Girart et al. (2012). In the three panels from Girart et al. (2012) the linearly polarized intensity is shown as color plots, while the contours represent the Stokes I emission (see Girart et al. 2012 for further details). While the JCMT/POL-2 data at this scale are prone to some beam-averaging, the polarization geometries between the continuum and line polarization are not consistent with a common origin. Note that the caption of Figure 2 in Girart et al. (2012) mislabels the SiS and CS images.

internal dissipation, to be aligned by some version of the RAT mechanism, or are aligned by the RAT-like mechanical alignment (MET) mechanism discussed by Lazarian & Hoang (2021), where gas particles reflect off of a helical grain surface and therefore align the grain’s angular momentum vector with the gas-dust drift velocity. MET alignment would, therefore, as would first-order k-RAT, produce azimuthal polarization in the AGB star envelope. However, given that only a small number of points show close to azimuthal polarization, neither first-order k-RAT nor MET-dominated alignment seem likely. As noted by Hoang & Lazarian (2009), weak “direct RAT alignment” can be achieved along the B field also without internal alignment, which for low- J attractor points can be with the long axis along the magnetic field.

Some level of internal alignment may be achieved from inelastic dissipation in porous grains (Purcell 1979; L. N. Tram 2022, private communications). This seems somewhat unlikely

in the IRC+10216 CSE, given the need to preserve large grains (Groenewegen 1997) under strong radiative disruptive driving (Hoang et al. 2019), which for porous grains with small tensile strength would result in the large aligned grains being destroyed. We note that the grain disruption is limited to grains at high- J attractor points (Lazarian & Hoang 2021), and a significant fraction of the dust may therefore not be affected by the disruption.

We are therefore left with magnetically aligned grains, possibly due to mineralogy changes or driven by grain charging and induced electric fields (Lazarian 2020) or some as yet unidentified grain alignment mechanism. Contamination by polarized line emission (J. Cernicharo 2021, private communications) also cannot be fully discounted at this stage, as discussed above.

Given the differences in polarization geometry between FIR and submillimeter-wave data, we used the Zeeman

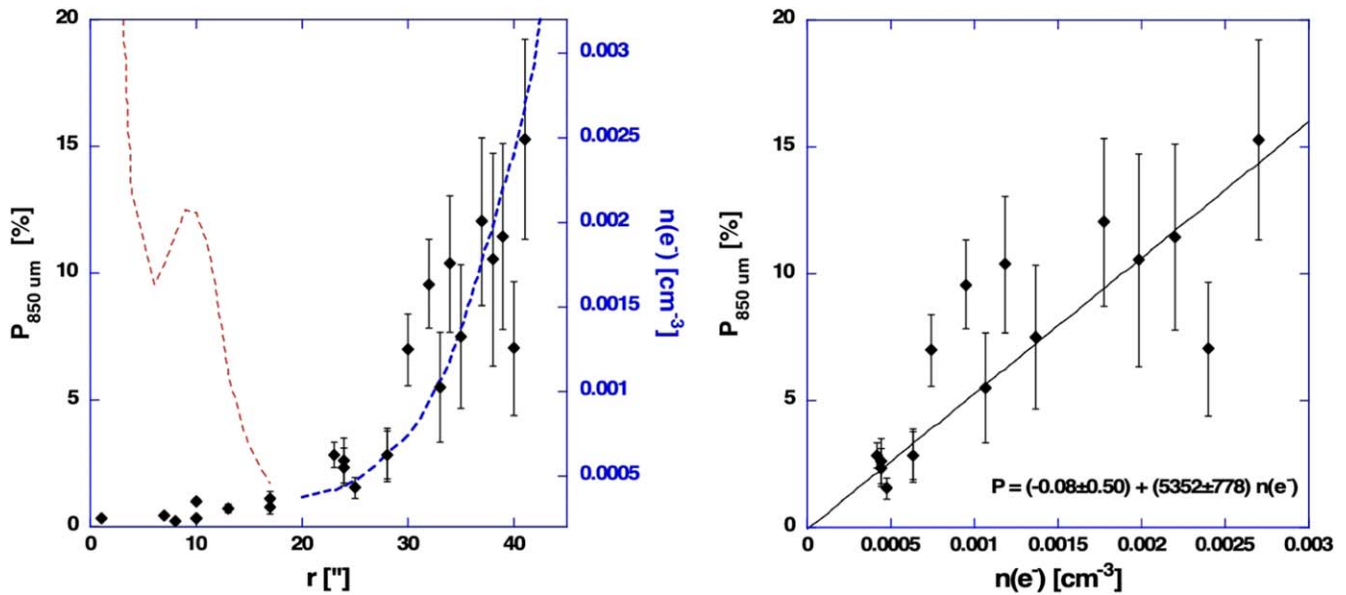


Figure 10. Left: The amount of $850\ \mu\text{m}$ polarization is well correlated with the electron density by photoionization due to the external diffuse radiation (UV) field (blue dashed line) calculated by Li et al. (2014) in the IRC+10216 envelope (the scaling of the two vertical axes has been arbitrarily set to show the correlation). The red dashed curve represents the modeled electron density generated by cosmic rays in the denser inner shell. As shown by Ivlev et al. (2015), grain charging by cosmic rays in the inner envelope (similar to their region “ \mathcal{I} ”) is inefficient. Right: A direct comparison between polarization and electron density for distances beyond $20''$ (where the latter is dominated by photoionization in the Li et al. 2014 models) yields a formally significant correlation.

observations from Duthu et al. (2017) to search for periodic variability in the line-of-sight magnetic field around the central star. While there are only five data points (plus an upper limit), we find a good fit to a cosine function of the azimuthal angle, Θ , around the star with the extremum located at $\sim 90^\circ$ – 125° . We interpret this as indicating a dipole pattern (being the second-order component of a spherical harmonics expansion). A dipole with its symmetry axis in the plane of the sky will not show any net line-of-sight polarization, since in the equatorial plane the B field is in the plane of the sky, while toward the poles there will be equal contributions of positive and negative fields along the line of sight (assuming optically thin emission). However, if the symmetry axis is tilted out of the plane of the sky, a net line-of-sight magnetic flux will result (as seen by, e.g., Vlemmings et al. 2005).

As our modeling (Figure 5) shows, a simple projected dipole model rotated by 125° east of north (E -vectors) yields a distinct nominal χ^2 minimum in the fit of the $850\ \mu\text{m}$ data, with a symmetry axis consistent with that implied by the Zeeman data. This provides some support for B-RAT alignment of the grains, or some other magnetically defined alignment mechanism giving rise to the $850\ \mu\text{m}$ polarization. As noted above, the large absolute minimum value of the reduced χ^2 means that a projected dipole is not, by itself, a complete or accurate model of the data. However, the localization of the symmetry axis seems to indicate that it likely forms part of the true polarization geometry.

It is noteworthy that Jeffers et al. (2014) have modeled the scattered light in the inner $\sim 3''$ of the IRC+10216 CSE as due to a torus centered on the star, with a symmetry axis of $\sim 75^\circ$ east of north. In our optical data, the only stars whose polarization diverges significantly from being azimuthal with respect to the central star IRC+10216 intercept this symmetry axis. If this represents the angular momentum/rotation axis of the CSE, it would imply a close alignment with the indicated magnetic axis.

5.1. Polarized Line-emission Contamination

While the nominal polarized line flux in the G-K polarization is similar to the SCUBA-2 polarized flux, the geometries of the two types of polarization do not seem consistent. Because the spatial sampling of the SMA and the JCMT are significantly different, we cannot conclusively rule out a measurable line polarization contamination in our data, but a dominant contribution from G-K polarization seems unlikely, because of the geometry. Simultaneous line and continuum polarization measurements of IRC+10216 with the Atacama Large Millimeter/submillimeter Array (ALMA) are planned for Cycle 10 to better address this issue.

5.2. Magnetic Dust Polarization Mechanisms

For dust polarization to be tracing a magnetic field in the CSE, the grains dominating the $850\ \mu\text{m}$ polarization must have acquired at least the equivalent of paramagnetic characteristics. This might be caused by variations in the grain chemistry with radius from the star, or with grain size (or some combination of these).

First, when considering the grain chemistry, the mineralogy of AGB envelopes naturally shows a radial variation due to the evolution on the AGB. As noted above, when a star first enters the AGB it is oxygen-rich. As the thermal-pulse-driven dredge-up of newly synthesized material is mixed up to the stellar surface and ejected into the CSE, it eventually becomes carbon-rich. This may leave silicate grains in the outer part of the CSE, with carbonaceous dust in the inner part of the envelopes, as reported for the planetary nebula BD+30°3639 (Guzman-Ramirez et al. 2015). The JCMT/POL-2 $850\ \mu\text{m}$ observations may therefore be tracing this outer, colder, fossil silicate dust seeing only dust at large distances from the star, even when projected close to the central star. However, because the emission is optically thin, the dominant contribution also to the $850\ \mu\text{m}$ Stokes I emission originates in the denser gas at

relatively small radii away from the central star. Given the expansion velocity of 14 km s^{-1} and distance of 123 pc, the presence of such fossil silicates would also require that the transition from oxygen- to carbon-rich chemistry would have been very recent, or that the mixing of the phases be very efficient (see Leão et al. 2006; Sahai & Chronopoulos 2010).

The possibility for explaining efficient alignment due to grain size, for the grains dominating at $850 \mu\text{m}$, parallels the proposed explanation of the shape of the optical polarization (“Serkowski”) curve under Davis–Greenstein (DG) alignment by Mathis (1986), using super-paramagnetic grain inclusions. The empirical Serkowski curve for diffuse ISM lines of sight requires that only grains with radii larger than $\sim 0.045 \mu\text{m}$ are aligned (Kim & Martin 1995). RAT alignment explains this as due to the lack of radiation below the Lyman limit in neutral gas (the condition for efficient RAT alignment being $\lambda < 2a$, where a is the effective grain radius). Because DG alignment becomes more efficient for smaller grains (e.g., Draine 2011), a mechanism was needed to deactivate it for grains smaller than this size. Because DG alignment further requires significantly higher magnetic susceptibility in the grains than for ordinary silicates (Jones & Spitzer 1967), Mathis (1986) proposed that the lack of small grain alignment was due to the fact that grains get aligned only if they contain at least one “super-paramagnetic inclusion” (of, for example, metallic iron, FeO, FeS, etc.; see Goodman et al. 1995). While mid-IR (MIR) observations show that the dust in the IRC+10216 CSE is fully carbonaceous (95% amorphous carbon and 5% SiC; Ivezić & Elitzur 1996a), iron is found to be depleted in the CSE gas (Mauron & Huggins 2010). It is therefore possible that the difference between FIR and submillimeter-wave polarization originates in differences in the alignment properties of smaller (and hotter) grains seen in the MIR/FIR, and larger (cooler) ones seen in the submillimeter, where the latter have acquired inclusions of, for example, ferromagnetic metallic iron or iron carbide (Fe_3C ; Wang et al. 2017). Since this is only a change in the alignment efficiency, it would not affect the Stokes I profile.

The fractional polarization, as a function of Stokes I intensity, shows a bimodal dependence in the $53 \mu\text{m}$ data, with a hint of a similar behavior at $154 \mu\text{m}$, indicating a change in alignment behavior at about $12''5$ from the star. Since the slope at higher intensities (closer to the star) is shallower and the absolute level is higher for this distribution than the steeper slope extending further out, this is unlikely to be due to radiative dust disruption (Hoang et al. 2019, 2021). Quantitative modeling will be needed to explore the origin of this bimodality, but does support a change in grain alignment physics with radius in the CSE.

5.3. Electrically Induced Alignment

Because of the cool photosphere of CW Leo²⁰ and the high column density of the CSE, the inner part of the envelope is expected to be close to neutral (modulo cosmic-ray ionization; Cordiner & Millar 2009), as supported by the strong absorption in KI (ionization potential of 4.3 eV) seen in “Star 6” of Mauron & Huggins (2010), even at an offset of $37''$ from the center of IRC+10216.

²⁰ For clarity, we refer to the central star by its name when specifically addressing stellar parameters, and “IRC+10216” for the extended object, including the star.

There is growing evidence for some kind of UV source at or close to the center of the CSE. Ionized carbon (through the $158 \mu\text{m}$ line of [C II]) has been observed with Herschel/HIFI toward the center of the CSE (Reach et al. 2022), as has the high- J line of HC_3N with ALMA (Siebert et al. 2022), which both require UV photons for their production. Based on imaging observations by Kim et al. (2015, 2021) and variability studies by, for example, Cernicharo et al. (2015), Decin et al. (2015), and Guélin et al. (2018), in their study Siebert et al. (2022) added a central UV source—most likely a “solar-like companion”—to their chemical modeling of the HC_3N abundance. The inner density peak of HC_3N resulting from this assumption is, however, located within a small enough radius ($\lesssim 5''$) that our observations would be significantly beam-averaged in this region.

For the outer parts of the CSE, UV photons from the diffuse interstellar field can penetrate the medium and ionize the gas, as well as charge the grains. While the work function for interstellar grains is not well known, the value of $W \approx 4.4 \text{ eV}$, appropriate for graphite (Weingartner & Draine 2001), is lower than the ionization potential of both hydrogen and carbon. Since both the grain charging and ionization fraction in the gas are due to the external UV field, we will therefore here use the gas electron density as a proxy for grain charge. As discussed above, the validity of this assumption depends on grain–electron collisions to be negligible. Figure 10 shows a clear correlation between the polarization fraction and electron density at offsets $\gtrsim 20''$ from the center of IRC+10216.

As discussed by Ivlev et al. (2015) and Ibáñez-Mejía et al. (2019), while the radiative grain charging at low extinctions for carbon grains is efficient, due to their low work function, the cosmic-ray grain charging (mostly through secondary H_2 UV emission in the Lyman and Werner bands) is less so, by at least an order of magnitude (see Figure 3 of Ibáñez-Mejía et al. 2019). This, possibly together with the beam-averaging at the very center, likely explains the lack of correlation between $n(e^-)$ and P inside $r \approx 20''$.

For emission polarimetry the polarization fraction P inherently has the appropriate line-of-sight averaging needed to address alignment effects (as noted by Hildebrand et al. 2000 for extinction and emission polarization, generally: $P_{\text{em}} = -P_{\text{ext}}/\tau$, where the minus sign denotes the fact that the emission and extinction polarization position angles are orthogonal). No significant correlation is seen between $n(e^-)$ and the polarized intensity, IP . Because of the nonuniform density structure (and spherical symmetry) of the CSE, our comparison is, of course, still only approximate, but points to a likely correlation between grain alignment and grain charging in the outer envelope.

As discussed above, Lazarian (2020) predicts that charged carbon grains with a net velocity perpendicular to the magnetic field should align with the magnetic and electrical fields (since the direction of the induced E field is given by the direction of the B field). If the precession rate around the E field (Ω_E) is faster than around the radiation field direction (Ω_k) and the B field (Ω_B), then theory predicts that the grains should align with their long axis parallel with the B field, and thence the observed emission polarization should be parallel to the B field. Since the polarization field (E -vector) symmetry, from our modeling, agrees with that from Zeeman data, our results indicate that this is the case ($\Omega_E > \Omega_B$). If confirmed, these results can therefore

provide constraints on the charging, drift velocity, and geometry of the grains.

To understand the dichotomy between FIR and optical polarization on the one hand and submillimeter-wave continuum polarization on the other in the envelope of IRC +10216, submillimeter observations at higher spatial resolution and better S/N are needed. Further, line and continuum polarimetry in the submillimeter-wave range acquired with the same instrument would be highly valuable to understand the relative contributions of dust and G-K polarization. The 7 m array of ALMA (and eventually the Morita array) can reach 4'' resolution for polarimetry at 870 μm —closely matching that of the SOFIA/HAWC+ 53 μm observations—and the high S/N needed to sensitively probe the cold dust in the inner (projected) part of the CSE.

The 3.4 μm aliphatic CH line is likely too inherently weak to be detectable in polarization in CSEs. (Chiar et al. (2000) reports line opacities of $\tau \sim 0.2$ toward the Galactic center for visual extinctions exceeding 30 mag.) However, the solid-state SiC line at 11.3 μm has been reliably detected in several carbon-rich CSEs (e.g., Sloan et al. 1998). Unfortunately, very little polarization data are available to specifically probe the alignment of such grains. The polarization data of Smith et al. (2000) may show a hint of polarization in this line for the carbon-rich post-AGB star AFGL 618 (showing a shape consistent with the flux spectra of carbon stars from Sloan et al. 1998). While the amplitude of this polarization line in AFGL 618 is only marginal with respect to its uncertainties, the possible detection of SiC polarization suggests that a systematic study of polarization in the line would be very valuable to further probe carbonaceous grain alignment.

6. Conclusions

We present 850 μm JCMT/SCUBA-2/POL-2 polarimetry of the CSE of the carbon-rich AGB star IRC+10216. In contrast to FIR 53 μm and optical polarimetry, which show an ordered radial (azimuthal) polarization pattern in the FIR (optical), implying dust grains aligned with their long axis in the radial direction away from the star, the submillimeter-wave polarization is more complex. Our data are not sufficiently extensive to allow a complete modeling of the 850 μm polarization data. However, based on an analysis of the Zeeman effect measurements in the CN ($J=1-0$) line by Duthu et al. (2017) and an assumption of the validity of a multipole decomposition of the magnetic field, we fitted a rotated, projected dipole to the 850 μm polarization data. Under this model assumption, a distinct preference for a symmetry axis is found, consistent with both the symmetry axis of the Zeeman results and the dust torus reported by Jeffers et al. (2014). These results imply that, if the polarization is due to aligned dust grains, the dust traced by submillimeter-wave observations is aligned with a magnetic field. The optical and FIR polarization, in contrast, indicate magnetically inactive dust aligned via a second-order pure radiative mechanism. To reconcile this dichotomy, we consider several possible explanations:

1. The 850 μm continuum polarization may be dominated by G-K line polarization, for example in the lines of CO ($J=3-2$), SiS ($J=19-18$), and CS ($J=7-6$), contained within the SCUBA-2 passband.

2. The cold dust probed by our 850 μm observations may have a different dust mineralogy than the dust probed by the optical and FIR observations. We hypothesize that this difference can arise from one of two processes:
 - (a) the submillimeter-wave data may be probing the fossil silicate dust from the oxygen-rich phase of the AGB star, located in the outer parts of the CSE; or
 - (b) the largest carbon grains may have acquired magnetically active inclusions from the depleted metals in the CSE (e.g., metallic iron or Fe_3C).
3. A new alignment mechanism (Lazarian 2020) applicable to charged grains with small magnetic susceptibilities (i.e., carbon grains) may explain our results, as the polarization fractions in the 850 μm data are well correlated with the calculated electron densities (Li et al. 2014) in the envelope.

Based on Occam's razor, the latter possibility is particularly attractive, as the FIR and submillimeter-wave polarization difference then is only a matter of differences in the grain charging state.

If the magnetic alignment of the grains seen at submillimeter wavelengths, and the dipole geometry of the resulting polarization, can be confirmed, the large-scale structure of the magnetic field around IRC+10216 will be known. The connection to the dust structures seen at small scales (Jeffers et al. 2014) is particularly intriguing.

Further continuum and line data at higher resolution and sensitivity, and preferably also at intermediate wavelengths, are needed to confirm and further explore these results. Our results indicate that pure carbon grains are likely not aligned in the ISM, and thereby provide observational constraints on the properties of composite grains (e.g., Draine & Hensley 2021).

Acknowledgments

B-G.A., A.S., and S.F.-M. gratefully acknowledge the support from the National Science Foundation under grant AST-1715876 and the SOFIA project under grant 05_0048. J.K. acknowledges funding from the Moses Holden Studentship in support of his PhD. M.T. is supported by the Banting Fellowship (Natural Sciences and Engineering Research Council Canada) hosted at Stanford University. Financial support for S.C. was provided by NASA through SOFIA award 08_0186 issued by USRA. We thank professor T. Miller for providing the data tables of electron density in the IRC+10216 shell and several helpful discussions. We thank Prof. J. Cernicharo for pointing out the possibility that our data are dominated by line polarization. We thank Prof. A. Lazarian and Dr. R. Sankrit for several insightful and helpful suggestions.

The James Clerk Maxwell Telescope is operated by the East Asian Observatory on behalf of The National Astronomical Observatory of Japan; Academia Sinica Institute of Astronomy and Astrophysics; the Korea Astronomy and Space Science Institute; Center for Astronomical Mega-Science (as well as the National Key R&D Program of China with No. 2017YFA0402700). Additional funding support is provided by the Science and Technology Facilities Council of the United Kingdom and participating universities and organizations in the United Kingdom and Canada. The authors wish to recognize and acknowledge the very significant cultural role and reverence that the summit of Maunakea has always had within the indigenous Hawaiian community. We are most fortunate to

have the opportunity to conduct observations from this mountain. Additional funds for the construction of SCUBA-2 and POL-2 were provided by the Canada Foundation for Innovation. This research used the facilities of the Canadian Astronomy Data Centre operated by the National Research Council of Canada with the support of the Canadian Space Agency.

This work is based in part on observations made with the NASA/DLR Stratospheric Observatory for Infrared Astronomy (SOFIA). SOFIA is jointly operated by the Universities Space Research Association, Inc. (USRA), under NASA contract NNA17BF53C, and the Deutsches SOFIA Institut (DSI) under DLR contract 50 OK 0901 to the University of Stuttgart.

Facilities: JCMT/POL-2, SOFIA/HAWC+.

Software: Astropy (Astropy Collaboration et al. 2013), Matplotlib (Hunter 2007), SciPy (Virtanen et al. 2020), NumPy (Harris et al. 2020), Starlink (Currie et al. 2014), SMURF (Chapin et al. 2011).

Appendix Dipole Model

The magnetic field model is based on a functional form described by King et al. (2018) to predict the polarization in synthetic MHD simulations. This model was then adapted to estimate the polarization from magnetically aligned dust grains in a torus by Lopez-Rodriguez et al. (2020). The implementation here has been simplified to model a rotationally symmetric dipole field.

For the magnetic field configuration, we assume a rotationally symmetric dipole of the form

$$B_r = -2 B_0 \cos(\phi + \psi), \quad (\text{A1})$$

$$B_\theta = -B_0 \sin(\phi + \psi), \quad (\text{A2})$$

where B_0 is proportional to r^{-2} , ϕ is the azimuthal angle, and ψ is the pitch angle of the dipole. This represents a somewhat simplified dipole for two-dimensional computation. In Cartesian coordinates, the field becomes

$$B_x = (-B_\theta \sin \phi) + (B_r \cos \phi), \quad (\text{A3})$$

$$B_y = (B_\theta \cos \phi) + (B_r \sin \phi), \quad (\text{A4})$$

$$B_z = B_0(r). \quad (\text{A5})$$

When this dipole is viewed at an inclination angle i and tilt Θ w.r.t. the plane of the sky, the observer's frame becomes

$$B_x^s = B_x \cos \Theta + (B_y \cos i - B_z \sin i) \sin \Theta, \quad (\text{A6})$$

$$B_y^s = -B_x \sin \Theta + (B_y \cos i - B_z \sin i) \cos \Theta, \quad (\text{A7})$$

$$B_z^s = B_y \sin i + B_z \cos i. \quad (\text{A8})$$

Following Lopez-Rodriguez et al. (2020), we then express the Stokes parameters in terms of the local magnetic field $B = (B_x, B_y, B_z)$ in the optically thin case $\tau_\lambda \ll 1$, for each point in a map on the sky of R.A., decl. (α, δ) :


$$I(\alpha, \delta) = \int n \left(1 - p_0 \left(\frac{B_x^2 + B_y^2}{B^2} - \frac{2}{3} \right) \right) ds, \quad (\text{A9})$$

$$Q(\alpha, \delta) = p_0 \int n \left(\frac{B_y^2 - B_x^2}{B^2} \right) ds, \quad (\text{A10})$$

$$U(\alpha, \delta) = p_0 \int n \left(\frac{2B_x B_y}{B^2} \right) ds, \quad (\text{A11})$$

where the x - and y -axes are in the plane of the sky, z is along the line-of-sight, and n describes the volume density. In our simulations, ds is along the z -axis. We implement n as a two-dimensional Gaussian function to generate an arbitrary “gas” volume density. p_0 relates dust grain cross sections with magnetic alignment properties. Because we are not here attempting to fit the polarization fraction, but only to fit the position angles between data and model, and because dipoles are rotationally symmetric, the density distribution in the model is not of primary importance. We note that because the model does not include quantitative polarized radiative-transfer calculations, we have limited our model fitting to the symmetric case with a zero inclination angle of the dipole axis, relative to the plane of the sky, i.e., a face-on view.

ORCID iDs

B-G. Andersson  <https://orcid.org/0000-0001-6717-0686>
 Janik Karoly  <https://orcid.org/0000-0001-5996-3600>
 Pierre Bastien  <https://orcid.org/0000-0002-0794-3859>
 Archana Soam  <https://orcid.org/0000-0002-6386-2906>
 Simon Coudé  <https://orcid.org/0000-0002-0859-0805>
 Mehrnoosh Tahani  <https://orcid.org/0000-0001-8749-1436>
 Michael S. Gordon  <https://orcid.org/0000-0002-1913-2682>

References

- Abbas, M. M., Tankosic, D., Craven, P. D., et al. 2006, *ApJ*, 645, 324
 Alves, F. O., Frau, P., Girart, J. M., et al. 2014, *A&A*, 569, L1
 Andersson, B. G., Hoang, T., Lopez-Rodriguez, E., et al. 2018, AAS Meeting, 231, 414.04
 Andersson, B.-G., Lazarian, A., & Vaillancourt, J. E. 2015, *ARA&A*, 53, 501
 Andersson, B. G., Lopez-Rodriguez, E., Medan, I., et al. 2022, *ApJ*, 931, 80
 Andersson, B.-G., Pintado, O., Potter, S. B., Straizys, V., & Charcos-Llorens, M. 2011, *A&A*, 534, A19
 Andersson, B.-G., & Potter, S. B. 2007, *ApJ*, 665, 369
 Andrae, R., Schulze-Hartung, T., & Melchior, P. 2010, arXiv:1012.3754
 Ashton, P. C., Ade, P. A. R., Angilè, F. E., et al. 2018, *ApJ*, 857, 10
 Astropy Collaboration, Robitaille, T. P., Tollerud, E. J., et al. 2013, *A&A*, 558, A33
 Bastien, P. 2003, in *Mass-losing Pulsating Stars and Their Circumstellar Matter*, ed. Y. Nakada, M. Honma, & M. Seki, 283 (Dordrecht: Kluwer), 181
 Bastien, P., Bissonnette, E., Simon, A., et al. 2011, in *ASP Conf. Ser. 449, Astronomical Polarimetry 2008: Science from Small to Large Telescopes*, ed. P. Bastien et al. (San Francisco, CA: ASP), 68
 Becklin, E. E., Frogel, J. A., Hyland, A. R., Kristian, J., & Neugebauer, G. 1969, *ApJL*, 158, L133
 Bevington, P. R., & Robinson, D. K. 1992, *Data Reduction and Error Analysis for the Physical Sciences* (2nd ed.; New York: McGraw-Hill)
 Bieging, J. H., Schmidt, G. D., Smith, P. S., & Oppenheimer, B. D. 2006, *ApJ*, 639, 1053
 Cernicharo, J., Marcelino, N., Agúndez, M., & Guélin, M. 2015, *A&A*, 575, A91
 Cernicharo, J., Waters, L. B. F. M., Decin, L., et al. 2010, *A&A*, 521, L8
 Chandrasekhar, S., & Fermi, E. 1953, *ApJ*, 118, 113
 Chapin, E. L., Chapman, S. C., Coppin, K. E., et al. 2011, *MNRAS*, 411, 505
 Chiar, J. E., Adamson, A. J., Whittet, D. C. B., et al. 2006, *ApJ*, 651, 268
 Chiar, J. E., Tielens, A. G. G. M., Adamson, A. J., & Ricca, A. 2013, *ApJ*, 770, 78
 Chiar, J. E., Tielens, A. G. G. M., Whittet, D. C. B., et al. 2000, *ApJ*, 537, 749
 Chuss, D. T., Andersson, B. G., Bally, J., et al. 2019, *ApJ*, 872, 187
 Cohen, M., & Schmidt, G. D. 1982, *ApJ*, 259, 693
 Cookson, J. L., Bintley, D., Li, S., et al. 2018, *Proc. SPIE*, 10708, 1070839
 Cordiner, M. A., & Millar, T. J. 2009, *ApJ*, 697, 68

- Cudlip, W., Furniss, I., King, K. J., & Jennings, R. E. 1982, *MNRAS*, **200**, 1169
- Currie, M. J., Berry, D. S., Jenness, T., et al. 2014, in ASP Conf. Ser. 485, *Astronomical Data Analysis Software and Systems XXIII*, ed. N. Manset & P. Forshay (San Francisco, CA: ASP), 391
- Davis, L. 1951, *PhRv*, **81**, 890
- De Beck, E., Lombaert, R., Agúndez, M., et al. 2012, *A&A*, **539**, A108
- Decin, L., Richards, A. M. S., Neufeld, D., et al. 2015, *A&A*, **574**, A5
- Decin, L., Royer, P., Cox, N. L. J., et al. 2011, *A&A*, **534**, A1
- Dharmawardena, T. E., Kemper, F., Scicluna, P., et al. 2018, *MNRAS*, **479**, 536
- Dolginov, A. Z., & Mitrofanov, I. G. 1976, *Ap&SS*, **43**, 291
- Drabek, E., Hatchell, J., Friberg, P., et al. 2012, *MNRAS*, **426**, 23
- Draine, B. T. 2011, *Physics of the Interstellar and Intergalactic Medium* (Princeton, NJ: Princeton Univ. Press)
- Draine, B. T., & Fraisse, A. A. 2009, *ApJ*, **696**, 1
- Draine, B. T., & Hensley, B. S. 2021, *ApJ*, **909**, 94
- Draine, B. T., & Lazarian, A. 1998, *ApJ*, **508**, 157
- Draine, B. T., & Weingartner, J. C. 1996, *ApJ*, **470**, 551
- Duthu, A., Herpin, F., Wiesemeyer, H., et al. 2017, *A&A*, **604**, A12
- Dyck, H. M., Forbes, F. F., & Shawl, S. J. 1971, *AJ*, **76**, 901
- Gail, H.-P., & Sedlmayr, E. 2013, *Physics and Chemistry of Circumstellar Dust Shells* (Cambridge: Cambridge Univ. Press)
- Girart, J. M., Patel, N., Vlemmings, W. H. T., & Rao, R. 2012, *ApJL*, **751**, L20
- Girart, J. M., Rao, R., & Marrone, D. P. 2006, *Sci*, **313**, 812
- Gold, T. 1952, *MNRAS*, **112**, 215
- Goldreich, P., & Kylafis, N. D. 1981, *ApJL*, **243**, L75
- Goldreich, P., & Kylafis, N. D. 1982, *ApJ*, **253**, 606
- Goodman, A. A., Jones, T. J., Lada, E. A., & Myers, P. C. 1995, *ApJ*, **448**, 748
- Groenewegen, M. A. T. 1997, *A&A*, **317**, 503
- Groenewegen, M. A. T., Barlow, M. J., Blommaert, J. A. D. L., et al. 2012, *A&A*, **543**, L8
- Guélin, M., Patel, N. A., Bremer, M., et al. 2018, *A&A*, **610**, A4
- Guzman-Ramirez, L., Lagadec, E., Wesson, R., et al. 2015, *MNRAS*, **451**, L1
- Hall, J. S. 1949, *Sci*, **109**, 166
- Harris, C. R., Millman, K. J., van der Walt, S. J., et al. 2020, *Natur*, **585**, 357
- Hildebrand, R. H., Davidson, J. A., Dotson, J. L., et al. 2000, *PASP*, **112**, 1215
- Hiltner, W. A. 1949a, *Sci*, **109**, 165
- Hiltner, W. A. 1949b, *ApJ*, **109**, 471
- Hoang, T., & Lazarian, A. 2009, *ApJ*, **697**, 1316
- Hoang, T., & Lee, H. 2020, *ApJ*, **896**, 144
- Hoang, T., Tram, L. N., Lee, H., & Ahn, S.-H. 2019, *NatAs*, **3**, 766
- Hoang, T., Tram, L. N., Lee, H., Diep, P. N., & Ngoc, N. B. 2021, *ApJ*, **908**, 218
- Holland, W. S., Bintley, D., Chapin, E. L., et al. 2013, *MNRAS*, **430**, 2513
- Houde, M., Vaillancourt, J. E., Hildebrand, R. H., Chitsazzadeh, S., & Kirby, L. 2009, *ApJ*, **706**, 1504
- Hunter, J. D. 2007, *CSE*, **9**, 90
- Ibáñez-Mejía, J. C., Walch, S., Ivlev, A. V., et al. 2019, *MNRAS*, **485**, 1220
- Ivezić, Z., & Elitzur, M. 1996a, *MNRAS*, **279**, 1019
- Ivezić, Z., & Elitzur, M. 1996b, *MNRAS*, **279**, 1011
- Ivezić, Z., Nenkova, M., & Elitzur, M. 1999, *DUSTY: Radiation Transport in a Dusty Environment*, Astrophysics Source Code Library, ascl:9911.001
- Ivlev, A. V., Padovani, M., Galli, D., & Caselli, P. 2015, *ApJ*, **812**, 135
- Jeffers, S. V., Min, M., Waters, L. B. F. M., et al. 2014, *A&A*, **572**, A3
- Jones, R. V., & Spitzer, L., Jr. 1967, *ApJ*, **147**, 943
- Jones, T. J., Bagley, M., Krejny, M., Andersson, B.-G., & Bastien, P. 2015, *AJ*, **149**, 31
- Kahane, C., Viard, E., Ménard, F., Bastien, P., & Manset, N. 1997, *Ap&SS*, **251**, 223
- Kastner, J. H., & Weintraub, D. A. 1994, *ApJ*, **434**, 719
- Kastner, J. H., & Weintraub, D. A. 1996, in ASP Conf. Ser. 97, *Polarimetry of the Interstellar Medium*, ed. W. G. Roberge & D. C. B. Whittet (San Francisco, CA: ASP), 212
- Kataoka, A., Tsukagoshi, T., Pohl, A., et al. 2017, *ApJL*, **844**, L5
- Khouri, T., Vlemmings, W. H. T., Paladini, C., et al. 2020, *A&A*, **635**, A200
- Kim, H., Lee, H.-G., Maunon, N., & Chu, Y.-H. 2015, *ApJL*, **804**, L10
- Kim, H., Lee, H.-G., Ohyama, Y., et al. 2021, *ApJ*, **914**, 35
- Kim, S.-H., & Martin, P. G. 1995, *ApJ*, **444**, 293
- King, P. K., Fissel, L. M., Chen, C.-Y., & Li, Z.-Y. 2018, *MNRAS*, **474**, 5122
- Kwon, J., Doi, Y., Tamura, M., et al. 2018, *ApJ*, **859**, 4
- Ladjal, D., Barlow, M. J., Groenewegen, M. A. T., et al. 2010, *A&A*, **518**, L141
- Lattanzio, J. C., & Wood, P. R. 2004, in *Asymptotic Giant Branch Stars*, ed. H. J. Habing & H. Olofsson (Berlin: Springer), 23
- Lazarian, A. 2020, *ApJ*, **902**, 97
- Lazarian, A., & Draine, B. T. 1999, *ApJL*, **516**, L37
- Lazarian, A., & Hoang, T. 2007, *MNRAS*, **378**, 910
- Lazarian, A., & Hoang, T. 2021, *ApJ*, **908**, 12
- Lazarian, A., Yuen, K. H., & Pogossyan, D. 2022, *ApJ*, **935**, 77
- Leão, I. C., de Laverny, P., Mékarnia, D., de Medeiros, J. R., & Vandame, B. 2006, *A&A*, **455**, 187
- Li, X., Millar, T. J., Walsh, C., Heays, A. N., & van Dishoeck, E. F. 2014, *A&A*, **568**, A111
- Liu, J., Qiu, K., Berry, D., et al. 2019, *ApJ*, **877**, 43
- Lopez-Rodriguez, E., Alonso-Herrero, A., García-Burillo, S., et al. 2020, *ApJ*, **893**, 33
- Lupton, R. 1993, *Statistics in Theory and Practice* (Princeton, NJ: Princeton Univ. Press)
- Mathis, J. S. 1986, *ApJ*, **308**, 281
- Mathews, B. C., McPhee, C. A., Fissel, L. M., & Curran, R. L. 2009, *ApJS*, **182**, 143
- Mauron, N., & Huggins, P. J. 1999, *A&A*, **349**, 203
- Mauron, N., & Huggins, P. J. 2000, *A&A*, **359**, 707
- Mauron, N., & Huggins, P. J. 2010, *A&A*, **513**, A31
- Medan, I., & Andersson, B.-G. 2019, *ApJ*, **873**, 87
- Milam, S. N., Woolf, N. J., & Ziurys, L. M. 2009, *ApJ*, **690**, 837
- Miller, J. S. 1970, *ApJL*, **161**, L95
- Min, M., Dullemond, C. P., Dominik, C., de Koter, A., & Hovenier, J. W. 2009, *A&A*, **497**, 155
- Montargès, M., Cannon, E., de Koter, A., et al. 2023, *A&A*, **671**, A96
- Murakawa, K., Suto, H., Oya, S., et al. 2005, *A&A*, **436**, 601
- Naghizadeh-Khouei, J., & Clarke, D. 1993, *A&A*, **274**, 968
- Olofsson, H. 2004, *Circumstellar Envelopes* (Berlin: Springer), 325
- Pattle, K., Lai, S.-P., Wright, M., et al. 2021, *MNRAS*, **503**, 3414
- Purcell, E. M. 1979, *ApJ*, **231**, 404
- Reach, W. T., Ruaud, M., Wiesemeyer, H., et al. 2022, *ApJ*, **926**, 69
- Sahai, R., & Chronopoulos, C. K. 2010, *ApJL*, **711**, L53
- Santos, F. P., Chuss, D. T., Dowell, C. D., et al. 2019, *ApJ*, **882**, 113
- Siebert, M. A., Van de Sande, M., Millar, T. J., & Remijan, A. J. 2022, *ApJ*, **941**, 90
- Sloan, G. C., Little-Marenin, I. R., & Price, S. D. 1998, *AJ*, **115**, 809
- Smith, C. H., Wright, C. M., Aitken, D. K., Roche, P. F., & Hough, J. H. 2000, *MNRAS*, **312**, 327
- Soam, A., Andersson, B. G., Straižys, V., et al. 2021, *AJ*, **161**, 149
- Szymczak, M., Cohen, R. J., & Richards, A. M. S. 2001, *A&A*, **371**, 1012
- Taberner, H. M., Dorda, R., Negueruela, I., & Marfil, E. 2021, *A&A*, **646**, A98
- Tahani, M., Bastien, P., Furuya, R. S., et al. 2023, *ApJ*, **944**, 139
- Trammell, S. R., Dinerstein, H. L., & Goodrich, R. W. 1994, *AJ*, **108**, 984
- Vaillancourt, J. E., & Andersson, B.-G. 2015, *ApJL*, **812**, L7
- Vaillancourt, J. E., Andersson, B.-G., Clemens, D. P., et al. 2020, *ApJ*, **905**, 157
- Vaillancourt, J. E., Dowell, C. D., Hildebrand, R. H., et al. 2008, *ApJL*, **679**, L25
- Virtanen, P., Gommers, R., Oliphant, T. E., et al. 2020, *NatMe*, **17**, 261
- Vlemmings, W. H. T. 2012, in IAU Symp. 287, *Cosmic Masers—from OH to H₀*, ed. R. S. Booth, W. H. T. Vlemmings, & E. M. L. Humphreys (Cambridge: Cambridge Univ. Press), 31
- Vlemmings, W. H. T., van Langevelde, H. J., & Diamond, P. J. 2005, *A&A*, **434**, 1029
- Wang, H. H., Li, G. Q., Ma, J. H., & Zhao, D. 2017, *RSCAd*, **7**, 44456
- Wardle, J. F. C., & Kronberg, P. P. 1974, *ApJ*, **194**, 249
- Weingartner, J. C. 2006, *ApJ*, **647**, 390
- Weingartner, J. C., & Draine, B. T. 2001, *ApJS*, **134**, 263
- Whittet, D. C. B. 2003, *Dust in the Galactic Environment* (2nd ed.; Bristol: IOP Publishing), 390
- Winters, J. M., Dominik, C., & Sedlmayr, E. 1994, *A&A*, **288**, 255